Faculty of Physics and Astronomy

University of Heidelberg

Diploma thesis

in Physics

submitted by

Friedhelm Serwane

born in Munich

2007

The setup of a Magneto Optical Trap for the preparation of a mesoscopic degenerate Fermi gas

This diploma thesis has been carried out by
Friedhelm Serwane at the
Max-Planck-Institute for Nuclear Physics
under the supervision of
Juniorprofessor Dr. S. Jochim

Abstract:

This thesis reports on the first steps towards the preparation of a mesoscopic degenerate Fermi gas with tunable interactions, opening a new field of model systems; intriguing prospects are the modelling of electrons in the atom or of nucleons in the core, respectively. The work emphasised on the development of a Magneto Optical Trap (MOT), in the course of which two aspects were crucial: Since a high loading rate of the MOT is required, the first goal of the work was to find a suitable design and implementation of the Zeeman slower as a source of slow atoms for the MOT. Additionally, a long lifetime for the few atom system and therefore an undisturbed environment of the atoms has to be guaranteed. Thus, the second goal of the thesis was to set up the vacuum system. Finally, a validation of the setup was made. The loading rate of the MOT was measured to $L \approx 10^9$ atoms/s at oven temperatures of $T = 400\,^{\circ}\mathrm{C}$ enabling short experimental duty cycles of few seconds which allows fast optimisation of experimental parameters. The lifetime of the atomic sample due to collisions with background gas atoms was determined to $\tau \approx 15$ minutes. According to this result, a long lifetime for the mesoscopic model system can be expected.

Zusammenfassung:

Diese Arbeit befasst sich mit den ersten Schritten hin zur Bereitung eines mesoskopischen, entarteten Fermigases mit einstellbaren Wechselwirkungen, welches einen neuen Bereich von Modellsystemen eröffnet; eine interessante Aussicht ist das Nachempfinden von Elektronen im Atom bzw. von Nukleonen im Kern. Der Schwerpunkt dieser Arbeit lag auf der Entwicklung einer magneto-optischen Falle (MOT), im Zuge derer zwei Aspekte entscheidend waren: Da eine hohe Laderate der MOT benötigt wird, bestand das erste Ziel der Arbeit darin, einen angemessenen Entwurf sowie eine Realisierung des Zeeman-Abbremsers als Quelle langsamer Atome für die MOT zu erarbeiten. Zusätzlich ist eine lange Lebensdauer des Systems und damit eine isolierte Umgebung der Atome sicher zu stellen. Daher war das zweite Ziel der Arbeit, das Vakuumsystem aufzubauen. Abschließend wurde eine Validierung der Apparatur vorgenommen. Für die Laderate der MOT wurde ein Wert von $L \approx 10^9$ Atomen/s bei Ofentemperaturen von $T = 400\,^{\circ}\mathrm{C}$ gemessen, was kurze Experimentierzyklen von wenigen Sekunden und damit eine schnelle Optimierung experimenteller Parameter ermöglicht. Die Lebensdauer der atomaren Probe belief sich unter Berücksichtigung von Stößen mit Restgasatomen auf $\tau \approx 15$ Minuten. Hinsichtlich dieses Ergebnisses kann eine lange Lebensdauer für das mesoskopische Modellsystem erwartet werden.

Contents

1. Introduction

Every time one succeeds in the preparation of a fundamental quantum mechanical system, it opens a door to explore further underlying phenomena. A prominent example is the Bose-Einstein condensation in the year 1995 [1]. After the successful establishing of a "clean" quantum system, experimentators used it more and more as a tool for the discovery of new fields such as matter wave interferometry [2].

Another fundamental system pictured in most of standard physics textbooks is the degenerate Fermi gas: Starting from the ground state, the energy levels are subsequently filled up with one identical fermion per state according to the Pauli principle until the Fermi energy is reached. This simple model successfully describes the properties of many systems in nature. An intriguing example are the nucleons in the core: Each nucleon occupies a single-particle state. Due to the fermionic nature of the particles, energy shells are formed. When a shell is filled, corresponding to a "magic number" of particles, the binding energy per particle becomes maximal. The same phenomenon exhibit other few fermion systems, e.g electrons of an atom trapped in the potential of the nucleus. An example for a macroscopic fermionic system are the neutrons forming a neutron star: Since they fill the energy states according to the Pauli principle, the system gets incompressible and thus stable against a collapse due to the strong attractive gravitational force. Having the fermionic nature in common, the systems differ from each other mainly by three properties: Firstly, the character of the potential holding the fermions together is different for each system. The electrons in an atom are attracted by 1/r Coulomb potential of the nucleus while the neutrons and protons in the nucleus are trapped by a potential according to the density distribution of the core. Secondly, the interaction properties between the fermions are different: In an atom, electrons interact via Coulomb repulsion, whereas the interactions of nucleons in the core are mediated by the strong force. Lastly, the particle number in different systems varies over many orders of magnitude from a helium nucleus with 2 protons and 2 neutrons to a neutron star consisting of a macroscopic number of particles.

The experimental realisation of a fermionic model systems became possible, when degeneracy of the Fermi gas could be reached via evaporative cooling of fermions [3]. By tuning the interaction properties of the fermions in the gas using Feshbach resonances, fermions could be paired. Those pairs revealed bosonic properties making molecular Bose-Einstein condensates possible [4][5][6]. Along with the ability to tune the fermionic interactions over a wide range from attractive to repulsive, model systems with macroscopic particle numbers were developed. The benefit was a better understanding of many phenomena, e.g superconductivity in solids [7]. The quality of a model system prepared in a laboratory strongly improve with its adaptability to different environments. In the recent past, techniques have been developed to provide the flexibility needed to establish appropriate settings: Since the successful confining of neutral atoms in optical dipole traps in 1986 [8], techniques have improved in various aspects: Via a better control of the laser light parameters, the properties of the trapping potential can be varied to a great extend. In the near future, nearly arbitrary potentials are feasible.
Those tools in hand, the goal of our experiment is the preparation of a mesoscopic degenerate Fermi gas with tunable interactions. This could open up a new field of model systems consisting of few fermions. In contrast to other experiments, one has not only the flexibility to simulate few fermionic systems, but also to observe the transition between few body and many body behaviours, such as BCS-like pairing, by increasing the particle number. The specific challenge in the preparation of such a sample is posed by the control of the small atom number: Few and well separated energy levels in the trap are required. Thus the level spacing has to be on the order of the Fermi energy. The trapping potential providing those properties will be created with a tightly focused optical dipole trap, which only allows a small numbers of fermionic states.

The thesis is structured as follows: The second chapter gives an introduction into the fundamentals of laser cooling and trapping with the emphasis on ^{6}Li. Importance is attached to the experimental parameters which optimise the performance of the Magneto Optical Trap. Subsequently, the experimental setup is described in chapter 3. The two main design parameters for our setup are a long lifetime of the trapped sample as well as a fast repetition rate for future experiments. The measurements of the important magnitudes, i.e the loading rate of the trap and the lifetime of the sample, are presented in chapter 4. Chapter 5 summarises the work and discusses first steps towards a mesoscopic model system.

2. Ultracold atoms

This chapter contains two parts: The first part gives a bief overview of atom-light interaction, in particular of neutral atoms in a laser field. The second part describes the use of this interaction for cooling and trapping as well as important design parameters for the Zeeman slower and the Magneto Optical Trap.

2.1. Principles of lasercooling

2.1.1. Atom-light interaction

When an atom interacts with an external laser field, two fundamental different absorption-emission cycles have to be distinguished:

1. Absorption of photons from the laser field and subsequent *stimulated* emission into the laser field as a coherent process.

2. Absorption of photons and subsequent *spontaneous* emission as an incoherent process.

Both the coherent and the incoherent process lead to a different kind of force acting on the atom, namely the *spontaneous force* and the *dipole force*. This can be explained by means of the Lorentz's model of the electon [10]: The electron is regarded as an oscillator elastically bound to the core. Its oscillation frequency ω_0 corresponds to the optical transition frequency of the atom. An electric field due to the laser

$$\mathbf{E}(\mathbf{r},t) = \hat{\mathbf{e}}\, E(\mathbf{r}) \exp\left(-i\omega t\right) + c.c. \tag{2.1}$$

drives the atom's electron at frequency ω inducing a dipole moment on the atom. The dipole moment oscillates at the same frequency as the driven electron giving

$$\mathbf{p}(\mathbf{r},t) = \hat{\mathbf{e}}\, p(\mathbf{r}) \exp\left(-i\omega t\right) + c.c.. \tag{2.2}$$

The oscillation amplitude p is related to the electric field via the complex polarisability

$$p = \alpha(\omega)E. \tag{2.3}$$

The model is convenient to derive formulas for the two resulting forces: While being accelerated by the laserfield, the oscillating electron looses energy due to dipole radiation at a classical rate

$$\gamma_\omega = \frac{e^2\omega^2}{6\pi\epsilon_0 m_e c^3}.$$

This leads to a damping term in the equation of motion

$$\ddot{x} + \gamma_\omega \dot{x} + \omega_0^2 x = -eE(t)/m_e. \tag{2.4}$$

The integration of equation 2.4 yields the amplitude and the phase of the oscillating dipole with respect to the driving field. This can be expressed in terms of the complex polarisability $\alpha(\omega)$

$$\alpha(\omega) = \frac{e^2}{m_e}\frac{1}{\omega_0^2 - \omega^2 - i\omega\gamma_\omega}. \tag{2.5}$$

$Re(\alpha)$ and $Im(\alpha)$ are related to the coherent process and incoherent process respectively for following reasons:

1. Coherent Process: The electric field drives the atomic transition coherently. The result is an interaction potential between the induced dipole moment $\mathbf{p}$ and the electric field $\mathbf{E}$

$$U_{\text{dipole}} = -\frac{1}{2}\langle \mathbf{pE} \rangle = -\frac{1}{2\epsilon_0 c} Re(\alpha) I \tag{2.6}$$

with laser intensity I.
$Re(\alpha)$ describes the strength of the in-phase oscillations of the dipole moment with the oscillations of the electric field. The related force, referred to as *dipole force*, is found by regarding the potential energy:

$$F_{\text{dipole}}(\mathbf{r}) = -\nabla U_{\text{dipole}}(\mathbf{r}) = \frac{1}{2\epsilon_0 c} Re(\alpha)\nabla I(\mathbf{r}). \tag{2.7}$$

Due to its dependence on the gradient of intensity, the *dipole force* can be used to trap neutral atoms in laserfields as briefly mentioned in section 5.

2. Incoherent Process: In the classical picture, the oscillator looses energy by dipole radiation leading to the damping term in equation 2.4. The power emitted by the oscillator and absorbed by the field is given by

$$P_{abs} = \langle \dot{\mathbf{p}}\mathbf{E} \rangle = 2\omega Im(pE^*) = \frac{\omega}{\epsilon_0 c} Im(\alpha) I. \tag{2.8}$$

The resulting scattering rate

$$\gamma(\mathbf{r}) = \frac{P_{abs}}{\hbar\omega} = \frac{1}{\hbar\epsilon_0 c} Im(\alpha) I(\mathbf{r}) \tag{2.9}$$

can be interpreted in terms of the rate of photons being spontaneously emitted into the laser field. The fact that the spontaneous emission happens isotropically, can be used to decelerate moving atoms. This is referred to as *spontaneous force* and will be discussed in the next section.

In general, the scattering rate γ depends on the detuning of the laser from the atomic resonance

$$\delta_0 = \omega - \omega_0$$

and the coupling strengths between the energy levels. To take this into account, a quantum mechanical approach has to be used: The atom's energy levels are quantised and coupled to the electric field. The resulting energies are eigenvalues of the total system, that is atom plus field. The corresponding eigenstates are referred to as *Dressed States*[11]. This leads to a set of coupled differential equations, the *Optical Bloch Equations*. Their solution yields the population probability ρ_{ee} of the excited state

$$\rho_{ee} = \frac{s_0/2}{1 + s_0 + (2\delta_0/\gamma)^2} \tag{2.10}$$

where

$$s_0 = \frac{2\,|\Omega|^2}{\gamma^2} = \frac{I}{I_s} \tag{2.11}$$

is called saturation parameter [12]. With the saturation intensity

$$I_s = \frac{\pi h c}{3\lambda^3 \tau}, \tag{2.12}$$

a scale for the laser intensity is introduced. For Intensities $I >> I_s$, one gets

$$\rho_{ee} = \rho_{gg} = 1/2$$

so that the maximum occupation number for the excited state can be reached. For ^{6}Li,

$$I_s = 2.54 \, \frac{\mathrm{mW}}{\mathrm{cm}^2}$$

which can be easily achieved with standard diode laser systems.

2.1.2. The spontaneous force

The absorption of a photon from the laserfield results in a momentum transfer

$$\Delta \mathbf{p}_{\mathrm{atom}} = \mathbf{p}_{\mathrm{photon}} = \hbar \mathbf{k} \tag{2.13}$$

to the atom. The subsequent spontaneous emission is isotropic, therefore the average momentum transfers of many cycles cancel each other out and the resulting momentum transfer is zero. Hence, the ***spontaneous force*** acting on an atom can be written as

$$\langle \mathbf{F} \rangle = \hbar \mathbf{k} \gamma_P \tag{2.14}$$

with the scattering rate

$$\gamma_P = \gamma \rho_{\mathrm{ee}} \tag{2.15}$$

proportional both to the natural linewith γ and the population of the excited state ρ_{ee}. The higher the occupation probability of the excited state is, the more photons can be exchanged with the ground state in an equilibrium and vice versa.

The dependence of ρ_{ee} on the detuning is shown in figure 2.1 for several saturation parameters s_0. At higher intensities, not only the transition at $\delta = 0$ is saturated, but also the wings of the distribution are strengthened. This yields a high scattering rate for slightly detuned atoms as well. For a typical experimental value

$$s_0 = 6,$$

which is obtainable with standard laser systems, the spectral distribution has a width of

$$\mathrm{FWHM}(s_0 = 6) \approx 2.6 \, \gamma.$$

The maximum force achievable is given by

$$F_{\mathrm{max}} = \frac{\hbar k \gamma}{2}. \tag{2.16}$$

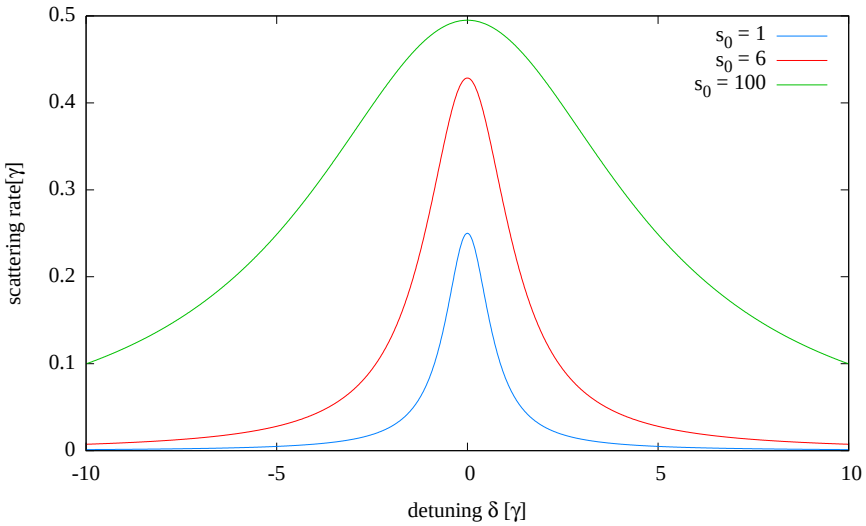

Figure 2.1.: *Power broadening of the spectral profile. The maximum of the scattering rate* $\gamma_p = \frac{1}{2}\gamma$ *is obtained in the high intensity limit. Because the wings of the distribution saturate for higher intensities, high scattering rates can not only be reached at* $\delta = 0$*: The atoms can be decelerated although they are not entirely on resonance. For a robust decelerating process, high saturation parameters are needed. In our Zeeman slower, the saturation parameter amounts to* $s_0 \approx 4$.

For ^{6}Li, $\gamma/2\pi \approx 5.87\,\mathrm{MHz}$, so a maximum deceleration

$$a_{\max} = \frac{\hbar k \gamma}{2m} \approx 2 \cdot 10^6 \frac{\mathrm{m}}{\mathrm{s}^2} \approx 200000\,\mathrm{g}$$

can be obtained.

2.1.3. Optical molasses

So far, only atoms at rest have been considered. To extend the concept to atoms moving with velocity $\pm\mathbf{v}$ in a laserfield with wave vector $+\mathbf{k}$ detuned by $\delta_0 = \omega - \omega_0$, the atom's effective detuning is shifted via the Doppler shift to

$$\delta_{v_\pm} = \delta_0 \mp kv. \tag{2.17}$$

The absolute value of the wave vector $\mathbf{k}$ can be expressed in terms of the laser frequency ω

$$|\mathbf{k}| = \frac{2\pi}{\lambda} = \frac{\omega_0}{c}. \tag{2.18}$$

For a counterpropagating laser beam, the Doppler shift is positive:

$$\delta_{v_-} = \delta_0 + \frac{v}{c}\omega. \tag{2.19}$$

In the case of two laserbeams with k-vectors $\pm\mathbf{k}$, the *spontaneous force* of both beams adds up to

$$\langle \mathbf{F} \rangle = \hbar\mathbf{k}\gamma_1 - \hbar\mathbf{k}\gamma_2 = \frac{\hbar k \gamma s_0}{2}\left(\frac{1}{1 + s_0 + \left(\frac{2\delta_{v+}}{\gamma}\right)^2} - \frac{1}{1 + s_0 + \left(\frac{2\delta_{v-}}{\gamma}\right)^2}\right) \tag{2.20}$$

For small Doppler shifts, equation 2.20 can be linearised to

$$\langle \mathbf{F} \rangle \cong \frac{8\hbar k^2 \delta_0 s_0}{\gamma(1 + s_0 + \left(\frac{2\delta_0}{\gamma}\right)^2)^2}\mathbf{v} \equiv -\beta\mathbf{v} \tag{2.21}$$

The net radiation force on an atom caused by two propagating laserbeams is shown in figure 2.2. For $\delta_0 < 0$, the force is directed in opposite direction of the atomic motion and since $\mathbf{F} \propto \mathbf{v}$, the motion of the atom is damped. For large detunings

$$\delta_0 >> \gamma$$

the force has two maxima at

$$v = \pm\frac{\delta_0}{k}$$

giving a maximum capture velocity.

Equation 2.21 is unphysical in so far as the atom will decelerate to $v = 0$ meaning $T = 0$. Considering a physical situation, a nonzero temperature can be explained in the following way: With every absorption of a photon, the atom is heated at least by the amount of the recoil energy

$$E_r = \frac{\hbar^2 k^2}{2m} = \hbar\omega_r.$$

When the atom emits one photon spontaneously, the same amount of energy is transferred to the atom. Within every cycle with two laser beams, the heating rate amounts to

$$2 \cdot 2\hbar\omega_r\gamma_p.$$

The temperature of the system can be estimated by equating the cooling rate $F(\delta) \cdot v$ [energy/s] with the heating rate $4\hbar\omega_r\gamma_p$ [energy/s] resulting in a temperature

$$k_B T = \frac{\hbar\gamma}{4}\frac{1 + (2\delta/\gamma)^2}{(|\delta|/\gamma)} \tag{2.22}$$

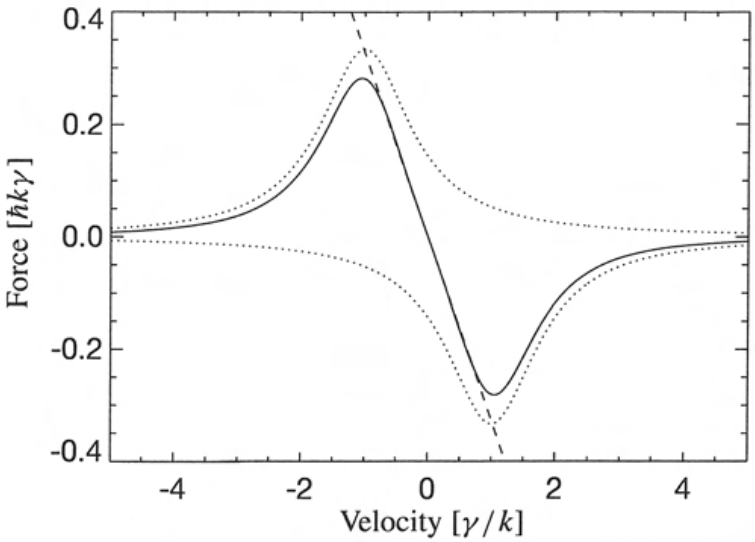

Figure 2.2.: *The addition of the spontaneous force from two counterpropagating laser beams results in a force* $\mathbf{F} = -\beta\mathbf{v}$ *forming an optical molasses. The maximum capture velocity is defined by the detuning* $v_c = \frac{\delta_0}{k}$*. Taken from [12].*

of an optical molasses. It has a minimum for

$$\delta = -\frac{\gamma}{2},$$

which sets a lower limit in temperature for this cooling method: the Doppler temperature

$$T_D = \frac{\hbar\gamma}{2k_B}. \tag{2.23}$$

For Lithium, the Doppler temperature has a value of

$$T_D \approx 140\,\mu K.$$

For larger detunings, the gradient β becomes smaller, so the cooling rate $F \cdot v$ decreases. This leads to an increase of the minimum temperature in the molasses. There exist methods for cooling below the Doppler temperature, e.g polarisation gradient cooling. Because of the low mass of Lithium, it has the largest recoil energy of all elements used for laser cooling. Its momentum spread at Doppler temperature $\sqrt{\langle p_z \rangle}$ is just as large as 5 recoil momenta and not much above the smallest momentum spreads achievable with sub-Doppler

cooling techniques [13]. For that reason, this thesis deals solely with the Doppler cooling technique.

With 6 counterpropagating laser beams, an optical molasses in 3 dimensions can be realized. It is referred to as *optical molasses* since the *spontaneous force* resembles the viscous drag on a body moving through molasses.

2.2. Applications of the light force

Both the Zeeman slower and the Magneto Optical Trap make use of the *spontaneous force* and the linear Zeeman effect for cooling, respectively trapping of atoms. For that reason, the Zeeman shift for ^{6}Li and the corresponding energy scales are briefly described before the concepts of Zeeman slower and MOT are explained.

Laser cooling of ^{6}Li

A closed transition of spontaneous emission and absorption is needed for populating the excited state continuously. Atoms with simple level schemes, well separated energy levels and few allowed dipole transitions are preferred. For atoms with more than one electron the dipole transition rule

$$\Delta j = \pm 1$$

changes to

$$\Delta \sum_{l_i} l_i = \pm 1.$$

That means, more dipole transitions with similar energies are allowed. Having only one valence electron and transitions in the visible range, alkalis are ideal candidates for lasercooling. Their number of *dark states*, i.e. hyperfine states outside the cooling cycle, is small.

Figure 2.3 shows the level scheme of ^{6}Li: The transitions from the ground state $^2S_{\frac{1}{2}}$ to the first exited states $^2P_{\frac{3}{2}}$, $^2P_{\frac{1}{2}}$ are known as the D_1 and D_2 line respectively with

$$\lambda \approx 671\,\mathrm{nm}.$$

For laser cooling, the D_2 line is used. Because of the large hyperfine splitting

$$\Delta E^{\mathrm{s}}_{\mathrm{HFS}}/h = 228\,\mathrm{MHz} \approx 40\,\gamma$$

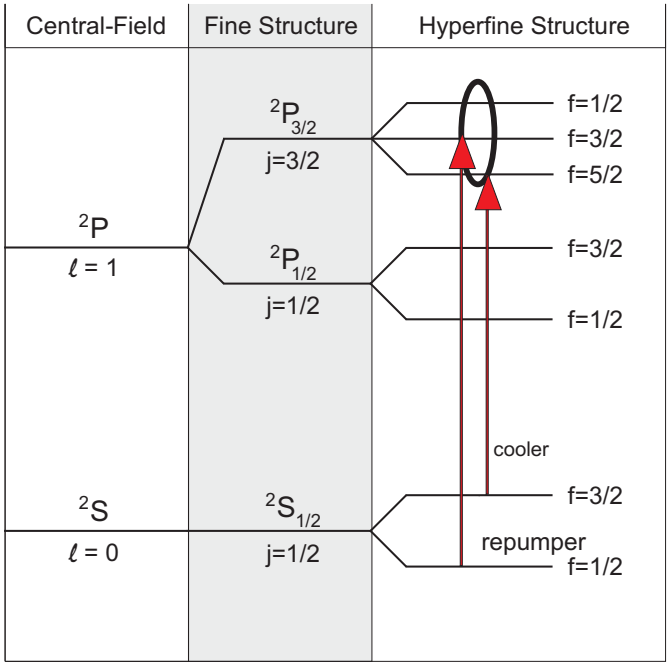

Figure 2.3.: *Levelscheme of* ^{6}*Li. Taken from [16].*

of the ground state and the small splitting of the excited state

$$E^{\mathrm{p}}_{\mathrm{HFS}} = O(1)\mathrm{MHz} < \gamma,$$

there exist two resolveable dipole transitions, from each energy level in the ground state to all energy levels in the excited state. To avoid atoms being emitted into the dark state with $\left|^2S_{\frac{1}{2}}, F = 1/2\right\rangle$, a repumper for this transition is needed.

2.2.1. Zeeman shifts and magnetic field regimes

As already mentioned in chapter 2.1.3, an atom moving in a counterpropagating laser beam has an effective detuning of

$$\delta_{\mathrm{v}} = \delta_0 + kv.$$

To excite the atom, the laser has to be red detuned

$$\delta_0 < 0.$$

For a decelerating atom, the effective detuning decreases and has to be compensated by some means.

One possibility is to shift the atom's energy levels via the linear Zeeman effect. The potential energy of an atom with total angular momentum

$$\mathbf{F} = \mathbf{I} + \mathbf{J}$$

in a magnetic field is given by

$$V^{\mathrm{HFS}} = -\boldsymbol{\mu}\mathbf{B} \tag{2.24}$$

with the atom's total magnetic moment

$$\boldsymbol{\mu}_F = \boldsymbol{\mu}_J + \boldsymbol{\mu}_I \tag{2.25}$$

where $\boldsymbol{\mu}_J$ is the total spin orbit angular momentum and $\boldsymbol{\mu}_I$ is the nuclear spin. Since both ground and excited states are shifted, the interesting energy shift is the difference

$$\Delta E^{\mathrm{HFS}} = -(\boldsymbol{\mu}_F^{\mathrm{ex}} - \boldsymbol{\mu}_F^{\mathrm{gnd}})\mathbf{B} \tag{2.26}$$

Two regimes can be distinguished depending on the strength of the external magnetic field: In the ***low field regime***, the coupling energy between nuclear spin $\mathbf{I}$ and spin-orbit $\mathbf{J}$ to

$$\mathbf{F} = \mathbf{J} + \mathbf{I}$$

is large compared to the energy of the atom in the external field B. Hence, the energy shift between ground and excited state can be written as

$$\Delta E^{\mathrm{HFS}}_{\mathrm{B,\,weak}} = \mu_B B(g_F^{\mathrm{ex}} m_F^{\mathrm{ex}} - g_F^{\mathrm{gnd}} m_F^{\mathrm{gnd}}) \tag{2.27}$$

with Landé factor

$$g_F = g_J \frac{F(F+1) + J(J+1) - I(I+1)}{2F(F+1)} + O(10^{-3} g_J). \tag{2.28}$$

This is referred to as the *Zeeman effect of the hyperfine splitting*. The dipole transition rules are

$$\Delta m_F = 0, \text{ (for } \sigma\text{-light: } \Delta F = \pm 1), \tag{2.29}$$

$$\Delta m_F = 1, \text{ (for } \pi\text{-light: } \Delta F = 0, \pm 1). \tag{2.30}$$

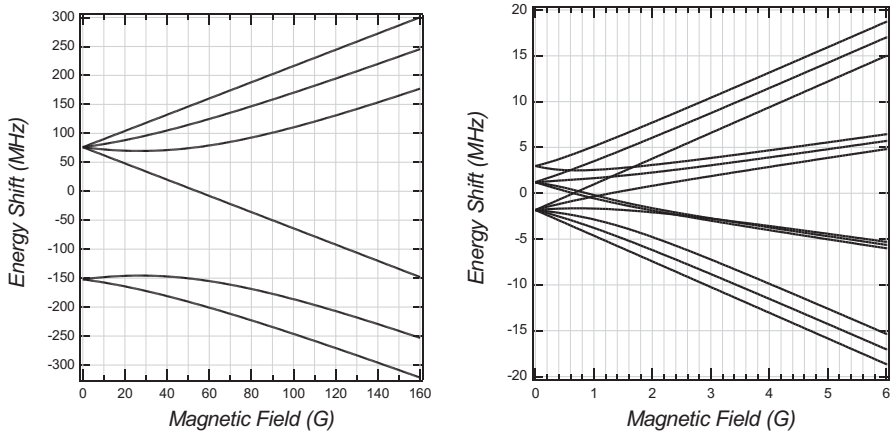

(a) Ground state of ^{6}Li. (b) Second excited state of ^{6}Li.

Figure 2.4.: *Zeeman splitting of ground and second excited state of* ^{6}*Li. When the external magnetic field is large compared to the coupling* $\mathbf{F} = \mathbf{I} + \mathbf{J}$*, the high field regime is reached. The ground state is in the high field regime for* $B \gtrapprox 100$ *Gauss whereas the high field regime for the second excited state already begins for values* $B \gtrapprox 3$ *Gauss. In the high field regime, the transitions used for laser cooling are closed, so no repumper is needed (see text). Taken from [16].*

In the ***high field regime***, i.e. when the energy of the atom in the external field is large compared to the coupling

$$\mathbf{F} = \mathbf{I} + \mathbf{J},$$

good quantum numbers are I and J and the energy shift is given by

$$\Delta E^{\mathrm{HFS}}_{\mathrm{B,\,strong}} = \mu' B + (A^{\mathrm{ex}} m_I^{\mathrm{ex}} m_J^{\mathrm{ex}} - A^{\mathrm{gnd}} m_I^{\mathrm{gnd}} m_J^{\mathrm{gnd}}) \tag{2.31}$$

with

$$\mu' = \mu_B (g_J^{\mathrm{ex}} m_J^{\mathrm{ex}} - g_J^{\mathrm{gnd}} m_J^{\mathrm{gnd}}).$$

A is the magnetic dipole constant of excited and ground state respectively. This behaviour can be treated as the *hyperfine structure of the Zeeman effect*. For this regime, the dipole transition rules are

$$\Delta m_J = \pm 1, \Delta m_I = 0 \tag{2.32}$$

$$\Delta m_I = \pm 1, \Delta m_J = 0 \tag{2.33}$$

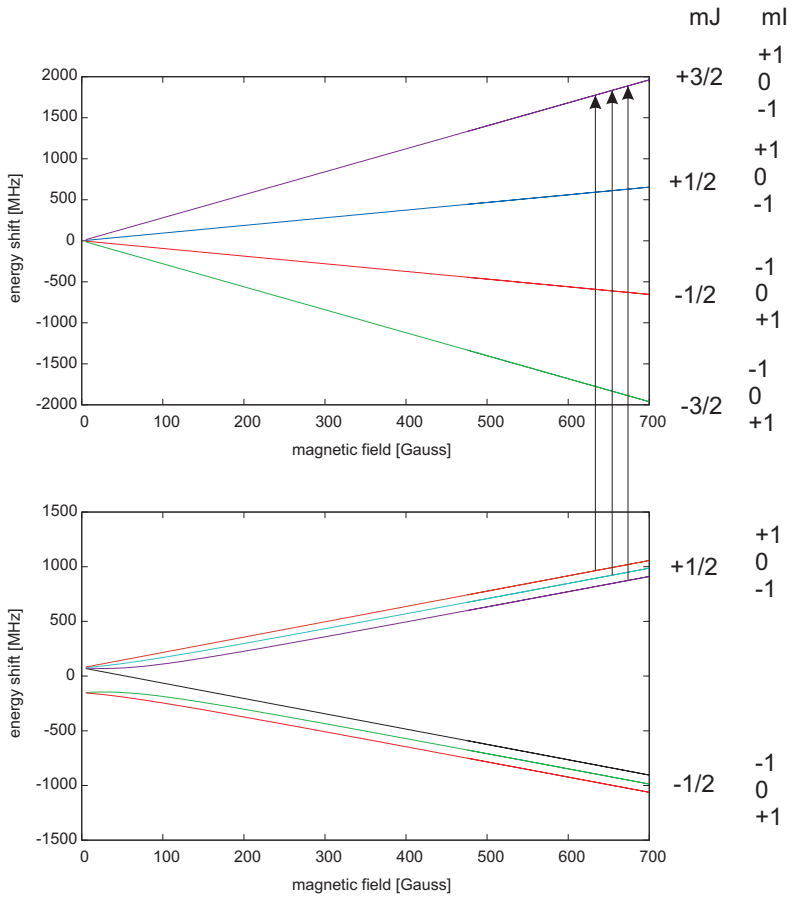

Figure 2.5.: *Zeeman splitting of the ground state* $2S_{3/2}$ *and the second excited state* $2P_{3/2}$ *of* ^6Li*. The energy level spacing between the magnetic sublevels with equal* m_J *is on the same order as the natural linewidth and not resolveable with our laser system. The three labelled transitions are used for cooling in the high field regime.*

Both regimes can be seen nicely in picture 2.4: The field strength required for the excited state to be in the high field regime is already reached at

$$B_{\text{high,ex}} \gtrapprox 3\,\text{Gauss}.$$

The required magnetic field strength for the ground state can be extracted from

figure 2.4 to

$$B_{\text{high},gnd} \gtrapprox 100\,\text{Gauss}.$$

One can also see from the selection rules 2.33 and figure 2.5, that the allowed dipole transitions from the ground state $\left|^2S_{\frac{1}{2}}, m_\text{J} = 1/2\right\rangle$ to the second excited state
$\left|^2P_{\frac{3}{2}}, m_\text{J} = 3/2\right\rangle$ are closed for fields $B_\text{high} \gtrapprox 100\,\text{Gauss}$.. That means for ^6Li, all three hyperfine sublevels $|m_\text{I} = +1, 0, -1\rangle$ can be used for cooling providing higher atomic fluxes in the MOT as described in chapter 2.2.2.

In the ***intermediate regime***, the behaviour of the energy levels is more complicated. In the special case where $F = I + \frac{1}{2}$, the energy shift can be described over the whole range of the magnetic field with the Breit-Rabi-formula

$$E = \frac{-A}{4} + m_F g_I \mu_K B \pm \frac{\Delta E_0}{2}\sqrt{1 + \frac{4m_F}{2I+1}x + x^2} \tag{2.34}$$

with

$$x = \frac{g_J\mu_B - g_I\mu_I}{\Delta E_0},\ \Delta E_0 = A(I + \frac{1}{2}).$$

In the case of ^6Li, the range of intermediate magnetic fields reaches from

$$3\,\text{Gauss} \gtrapprox B \gtrapprox 100\,\text{Gauss}.$$

Since neither F nor J and I are appropriate quantum numbers here, possible transitions are hard to predict. For efficiently cooling of the atoms with a Zeeman slower, it is desirable to work in a regime where the transitions are known to be closed as it is the case in the high field regime. This will be discussed in the following section.

2.2.2. The Zeeman slower

A Zeeman slower is used to decelerate thermal atoms from thermal velocities $v \approx 1000\,\text{m/s}$ to a few m/s. Atoms with velocity $-\mathbf{v}_\text{initial}$ are slowed down by the *spontaneous force* imposed by a red detuned counterpropagating laser beam with k-vector $+\mathbf{k}$.

Magnetic fields

Including the atom's potential energy in the magnetic field results in the atom's effective detuning from resonance

$$\boxed{\delta_{\text{eff}} = \delta_0 + \frac{v}{c}\omega - \frac{\Delta E^{\text{HFS}}}{\hbar} \approx \delta_0 + \frac{v}{c}\omega - \frac{\mu' B}{\hbar}}. \tag{2.35}$$

To maintain a scattering rate high enough to keep the atom in the cooling cycle, the value of δ_{eff} should be on the same order as the full width half maximum (FWHM) of the spectral intensity shown in figure 2.1. The decreasing velocity with respect to the position of the atom is given from kinematics:

$$v^2(z) = v_{\text{initial}}^2 - 2a_{\max} z. \tag{2.36}$$

Combining equations 2.35 and 2.36 shows the spatial dependence of the magnetic field

$$B(z) = \frac{\hbar}{\mu'}(\delta_0 + \frac{\omega}{c}\sqrt{v_{\text{initial}}^2 - 2a_{\max} z}). \tag{2.37}$$

Possible Zeeman slower configurations

Our main design goal for the Zeeman slower is a high atomic flux at a simple design. The free parameters of formula 2.37, namely the combination of magnetic fields/detuning and length, are chosen according to the mentioned prerequisite. In the following, the influence of these parameters on the flux are discussed. The highest atomic flux can be reached, when the end of the slower coincides with the centre of the MOT as shown in figure 2.7. This requires the magnetic field of the Zeeman slower to overlap smoothly with the MOT field. In principle, 3 different combinations of magnetic field configurations and detunings are possible as shown in figure 2.6.

1. An ***increasing field*** Zeeman slower has its highest magnetic fields near the centre of the MOT and the laser is resonant with atoms at velocities $v = v_{\max}$. The advantage of this setup is, that the laser can be detuned very far from the atomic transition. In the given example in figure 2.6, values reach from

   $$\delta_0 = -1.3\,\text{GHz} \approx 36\,\gamma.$$

   By that means, scattering of the atoms in the MOT by the Zeeman slower laser beam is strongly suppressed, so dissipative heating processes are reduced. At the same time, the high magnetic fields (up to 800 Gauss in

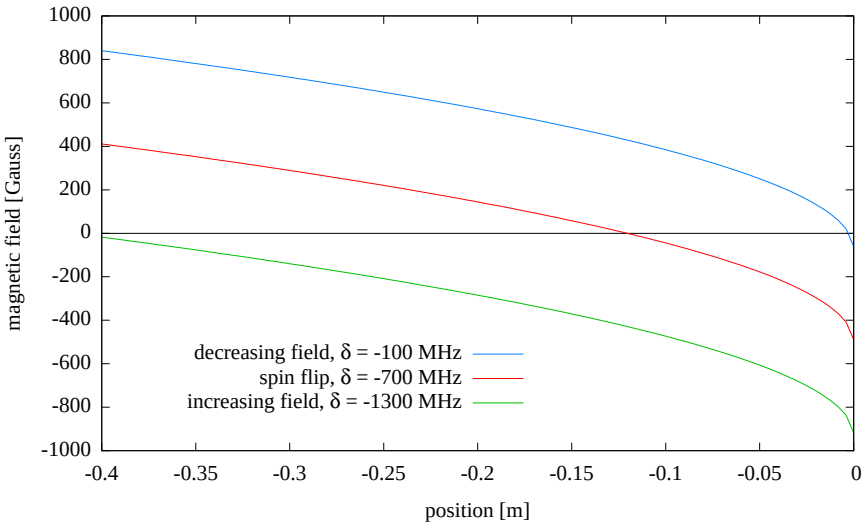

Figure 2.6.: *Possible Zeeman slower configurations. Depending on the magnetic fields and detuning, the three configurations shown are possible. To prevent the atoms from being accelerated into the Zeeman slower again, they have to be nonresonant to the laser light at the end of the slower. Therefore, the magnetic field has no zero crossing in the decreasing field configuration.*

the example) close to the MOT cause two disadvantages: First of all, a compensation coil is needed to ensure an abrupt drop-off of the Zeeman slower towards the centre of the MOT. An overlap with the magnetic field of the MOT is hardly achievable. Secondly, as most of the heat is produced near the experimental chamber, this may increase the pressure in the vacuum chamber without an involved cooling mechanism.

2. A ***spin flip*** configuration has several advantages: smaller total magnetic fields are needed than in the other configurations and high detunings from the MOT lasers are possible. From equation 2.35, it is clear that the position of the zero crossing of the magnetic field is determined by the value of the detuning δ_0. For larger detunings, the atoms are required to pass the zero crossing of the magnetic field at higher velocities. This leads to a disadvantage of a spin-flip Zeeman slower: In the *high field regime*

$$B \gtrapprox 100\,\text{Gauss},$$

the cooling transitions are always closed as discussed in the last section.

In the *intermediate regime*

$$|B| < 100\,\text{Gauss},$$

one cannot expect the transitions to be closed, so atoms can possibly fall into the dark state $\left|^2S_{1/2}, F = 1/2\right\rangle$. As mentioned in above, a repump laser is used to bring the atoms from the state $\left|^2S_{1/2}, F = 1/2\right\rangle$ back into the cooling cycle. When the repump laser frequency is chosen according to the hyperfine splitting of the ground state, i.e. 228 MHz larger than the cooling frequency, the concept of repumping only works for small magnetic fields where the repumper is still resonant. To estimate the magnetic field range, within repumping is still possible, one has to consider the spectral profile of the repump laser. At experimental values for the intensity of the Zeeman slower laser of $s_0 = 6$, the width of the spectral profile can be extracted from figure 2.1 to

$$\text{FWHM}(s_0 = 6) \approx 2.6\,\gamma \approx 15\,\text{MHz}.$$

Let us assume, the repump laser can still excite enough atoms detuned by an amount of ± 15 MHz. From the equations for the low field 2.27 and from figure 2.5, one can determine the magnetic field range, where the repumper still works to

$$B < 5\,\text{Gauss}.$$

Only within this regime, atoms in the dark state $\left|^2S_{1/2}, F = 1/2\right\rangle$ can be repumped into the cycling process. In the intermediate regime, the repumper is not on resonance with the atoms. In addition, the intermediate regime for a spin-flip configuration is double as large as for a decreasing field configuration:

$$|B| \lessapprox 100\,\text{Gauss}.$$

That means, that over a range of 200 Gauss, there is always a certain possibility for the atoms to fall into the dark state. When the atom falls into the dark state at too high velocities, it cannot be decelerated further and is not trapable by the MOT anymore. Even an increase in intensity by a factor of 10 would broaden the magnetic field regime to $B < 20\,\text{Gauss} << B_{\text{strong}}$. For those reasons, we decided in favour of a decreasing field configuration:

3. In a ***decreasing field*** configuration, the detuning from the atomic resonance is small:

$$\delta \approx 100\,\mathrm{MHz} \approx 16\,\gamma.$$

To avoid the acceleration of already slow atoms into the slower, the decelerated atoms have to get off resonance with the decelerating laser beam after leaving the Zeeman slower. This is realised by a decrease of the magnetic field to zero towards the centre of the MOT instead of changing the sign of the magnetic field. At fields

$$B > 100\,\mathrm{Gauss},$$

the cooling transitions are closed due to the selection rules for the high field regime 2.33, so no repump laser is needed here. In the intermediate regime, a repumper *can* help, but this is not obvious, since the selection rules are complicated. In the low field regime, where the repumper would be resonant, the magnetic field range is as small as $B < 5\,\mathrm{Gauss}$. In this regime, the atoms are already so close to the MOT centre

$$d \approx 5\,\mathrm{mm},$$

that they interact with the MOT repumpers. The amount of heat produced by the magnetic field coils can be conducted with some effort, but this is uncritical since the distance between experimental chamber and hottest coil is large. In a decreasing field configuration, small detunings are possible

$$\delta \approx 100\,\mathrm{MHz} \approx 16\,\gamma,$$

but figure 2.1 shows that the scattering rate with

$$\gamma_p(\delta = 100\,\mathrm{MHz}) = 10^{-3}\,\gamma$$

can be neglected at a typical saturation parameter

$$s_0 = 6.$$

Dependence of the flux on the length

In a Zeeman slower, the atom has to be decelerated until

$$v_{\mathrm{final}} < v_{\mathrm{c}}^{\mathrm{MOT}}$$

with v_c being the capture velocity of the MOT. From equation 2.36, we get the maximum capture velocity of the Zeeman slower

$$v_{max} = \sqrt{v_{final}^2 + 2aL}. \tag{2.38}$$

A longer slower increases the number of slowed atoms but decreases the solid angle of trappable atoms for the MOT. Following the ideas of the John Thomas' group[17], one can estimate this effect: The atomic flux of atoms leaving the oven is limited by the oven's aperture with surface A and can be estimated to

$$I_{oven} = \frac{n\overline{v}A}{4} \tag{2.39}$$

where

$$n = \frac{p}{kT}$$

is the atomic density at vapour pressure p and the atom's mean velocity $\overline{v} = \sqrt{\frac{2kT}{m}}$. With typical values for the temperature $T = 400$℃, the mean velocity for ^{6}Li becomes $\overline{v} = 1540\,\frac{m}{s}$. In our case, the large aperture of the oven

$$A = (5\text{mm})^2\pi$$

leads to an atomic flux of

$$f_{oven} = 4 \cdot 10^{16}\,\frac{\text{atoms}}{\text{s}}. \tag{2.40}$$

The Maxwell Boltzmann distribution describes the velocity distribution of the escaping atoms both in longitudinal and transversal direction. The number of atoms leaving the oven with directions given by θ and ϕ with velocity v is [18]

$$d\dot{N}_{v,\theta,\phi} = \frac{nA}{\pi^{3/2}\overline{v}^3} v \exp\left(\frac{-v^2}{\overline{v}^2}\right) \cos\theta v^2 \sin\theta dv d\theta d\phi. \tag{2.41}$$

Only atoms with axial velocity $v_z < v_{z,max}$ can be trapped in the MOT. The atoms are cooled in the longitudinal direction only. This leads to a divergence of the atomic beam after a certain time of flight. When the divergence is larger than the capture radius of the MOT, the flux of trappable atoms is reduced: Only atoms with a small transversal velocity can be trapped. The maximum transversal velocity v_r depends strongly on the atoms time of flight in the apparatus:

$$v_r \leq v_{r,max} = \frac{r_0}{t_{before} + t_{during} + t_{after}} \tag{2.42}$$

with the MOT's capture radius $r_0 \approx 1\text{cm}$, the atom's time of flight before the slower t_{before}, in the slower t_{during} and after t_{after} the slower into the centre of the MOT. The atom's time of flight after the slower into MOT is given by

$$t_a = \frac{d_a}{v_{\text{end}}}$$

where d_a is the dead space between the end of the Zeeman slower and the centre of the MOT. The atom's time of flight in the slower t_d can be calculated from kinematics to

$$t_d = \frac{1}{a}(\sqrt{v_{\text{final}}^2 + 2aL} - v_{\text{final}}). \tag{2.43}$$

At thermal velocities, t_b can be neglected, while t_a is critical: While $v_z \approx 50\,\text{m/s}$, the atoms longitudinal velocity is small compared to nearly thermal transversal velocities $v_{\text{r}} \approx 1000\,\text{m/s}$. That means for a dead space $d_a = 1\,\text{cm}$ the atom already needs $t_a = 0.2\,\text{ms}$ to reach the centre of the MOT. During that time, the atom travels $r = 0.2\,\text{m}$ in radial direction and is therefore untrappable by the MOT. This leads to a drop in atomic flux.

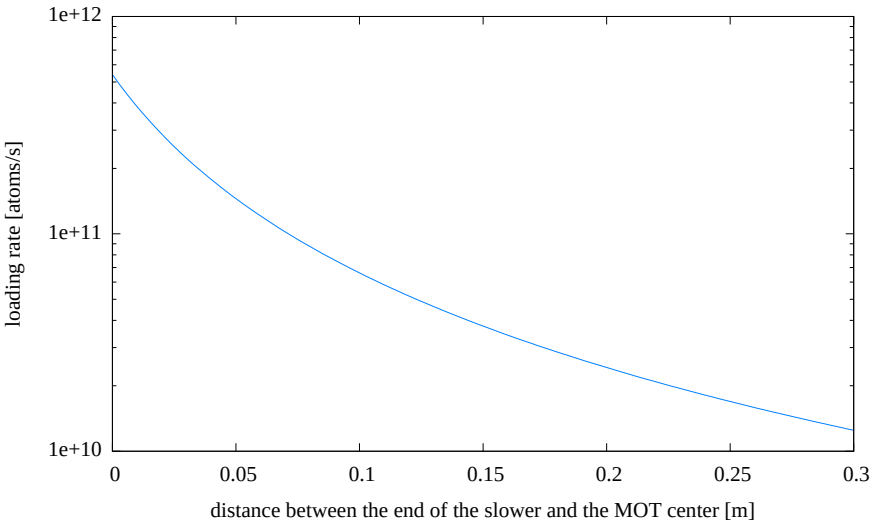

Figure 2.7.: *Dependence of the loading rate on the distance between Zeeman slower and centre of the MOT calculated for experimental values of our slower. After leaving the Zeeman slower, the atom's longitudinal velocity is reduced to $v_l \approx 50\,m/s$ while its transversal velocity is still comparable to thermal velocities. The longer the atom's time of flight after the Zeeman slower is, the more atoms escape the MOT's capture radius.*

For those reasons, it is crucial that the end of the Zeeman slower is located as close as possible to the centre of the MOT.

The total number of atoms/second trappable by the MOT can be calculated by performing the integrals of equation 2.41 over angles and velocities using the limits for v_{rmax} and v_{zmax} [17].

$$f = f_{\mathrm{oven}}(1 - e^{-\frac{v_{\mathrm{rmax}}^2}{\bar{v}^2}})(1 - e^{-\frac{v_{\mathrm{zmax}}^2}{\bar{v}^2}}). \tag{2.44}$$

The expected flux for our parameters is plotted in figure 2.8. A slower with $l = 40\,\mathrm{cm}$ operating at $T = 400\,^{\circ}\mathrm{C}$ is long enough to provide maximum atomic fluxes on the order of $f \approx 10^{12}\,\frac{\mathrm{atoms}}{\mathrm{s}}$. Higher fluxes can be reached by transversal laser cooling during the deceleration stage of the atoms (2-D MOT).

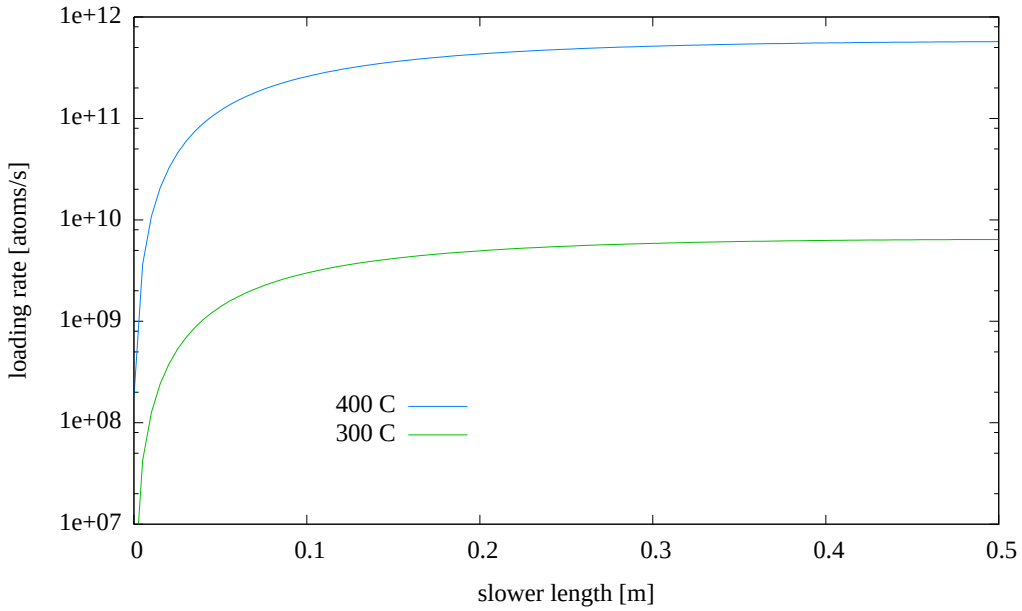

Figure 2.8.: *Dependence of the loading rate on the length of the Zeeman slower. A longer slower allows higher capture velocities and increases the atomic flux. At the same time, the solid angle of trappable atoms gets smaller with a longer slower. Neglecting transversal heating and other loss processes, a slower with $l = 40\,cm$ and $T = 400\,^{\circ}C$ is long enough to provide atomic fluxes on the order of $f \approx 10^{12}$ atoms/second. Parameters used: $v_{\mathrm{end}} = 50\,m/s$, dead space after the slower $d_a = 0\,cm$ (should be as small as possible, see figure 2.7), effective deceleration $a = 1/2\,a_{\mathrm{max}}$, capture radius of the MOT $r_c = 1\,cm$*

In this approximation transversal heating due to spontaneous emission during

the deceleration process is completely neglected. Including this effect spreadens the atomic beam even more. According to this approximation and for our experimental parameters, the ratio

$$\frac{I_{\mathrm{L=1m}}}{I_{\mathrm{L=0.4m}}} \approx 1.$$

This is an argument for a short slower. When transversal heating is included, the ratio is expected to be even better, because the divergence of the atomic beam is larger for a longer slower. In summary, the advantage of an easy to implement 0.4 m long Zeeman slower with moderate magnetic fields outweights the disadvantage of a longer setup.

2.2.3. The Magneto Optical Trap

A Magneto Optical Trap (MOT) combines confinement in velocity space provided by an optical molasses with confinement in real space: A linearly rising magnetic field creates a spatial dependence of the scattering rate and therefore a spatial dependence of the spontaneous force. To address only atoms moving away from the trap centre, counterpropagating circular polarised laser beams are used. Figure 2.9 explains the details.

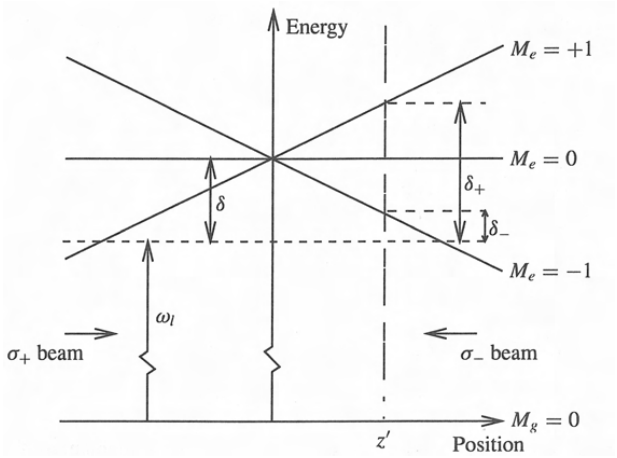

Figure 2.9.: *Atoms at a position z' scatter more photons out of the σ^- beam than the σ^+ beam because the effective detuning δ_- for the $M_e = -1$ state is smaller than the effective detuning δ_+ for the $M_e = 1$ state. Therefore the δ_- beam drives the atom to the centre of the trap. Taken from [12].*

The atom's effective detuning including the magnetic field

$$\delta_{eff\pm} = \delta_0 \pm kv \mp \frac{\mu' B}{\hbar}$$

has already been introduced in section 2.2.2. With the expression for δ_{eff}, the *spontaneous force* acting on an atom for small Doppler and Zeeman shifts is proportional both to the velocity and the position of the atom

$$\langle \mathbf{F} \rangle \cong -\beta \mathbf{v} - \kappa \mathbf{r} \tag{2.45}$$

with damping coefficient

$$\beta = \frac{8\hbar k^2 \delta_0 s_0}{\gamma(1 + s_0 + (\frac{2\delta_0}{\gamma})^2)^2}$$

and spring constant

$$\kappa = \frac{\mu' A}{\hbar k}\beta$$

where $A = \frac{\partial B}{\partial z}$ is the gradient of the magnetic field.

The trajectories caused by force 2.45 are a damped harmonic motions of the atoms towards the centre of the trap at oscillation frequency

$$\omega_0 = \sqrt{\kappa/m}.$$

For a Lithium MOT, the damping rate typically amounts

$$\gamma = \frac{\beta}{m} = O(10^4)\,\text{Hz},$$

which is larger than the typical oscillation frequency ω_0 of the atoms in the MOT. That means the atomic motion is overdamped. Typical restoring times are in the range of

$$\tau \approx 0.1\,ms.$$

A good overview over the dynamics in a MOT is presented in the PhD Thesis of Jochen Steinmann [15].

Loading rate and total atom number

The total atom number N in a MOT is determined by the equilibrium of atoms loaded from the Zeeman slower and loss mechanisms. For that reason, the atom number in the MOT can be described with following rate equation

$$\frac{dN}{dt} = L - RN - \beta \int n(r)^2 \, d^3r \tag{2.46}$$

where L is the loading rate in atoms/s and R is the one-body loss rate per atom due to collisions with background gases. The term proportional to n^2 describes the losses due to inelastic collisions of the trapped atoms. When a gaussian shape of the atomic cloud is assumed, the two-body loss term in equation 2.46 can be simplified to

$$\beta' N^2 = \frac{\beta}{(\pi/2)^{\frac{3}{2}} \sigma_z \sigma_r^2} N^2 \tag{2.47}$$

with $1/\sqrt{e}$ width in radial σ_r and axial σ_z direction. The two main two-body loss processes are [21]:

1. *Radiative escape*: A radiative escape can occur when an atom in the ground state S collides with an atom in the excited state P. During the collision process, a quasi-molecule $S - P$ with an attractive potential

   $$V(r) \propto -1/r^3$$

   is formed. The atoms are accelerated towards each other until the excited atom emits a redshifted photon spontaneously. The two atoms end up in the flat ground state potential $S - S$, but still have the kinetic energy gained from the attractive potential. By that means energy from the lightfield is converted into kinetic energy of the atoms leading to an *radiative escape* of the atoms from the trap.

2. *State changing collisions*: When two atoms collide and the electronic structure of one or both atoms is changed during the collision, the energy difference between initial and final state is converted into kinetic energy. At energy differences higher than the trap depth, the atom can escape from the trap.

For our setup, the losses due to atom-background collisions are only visible at low densities where the two-body losses can be neglected. In this limit, equation 2.46 can be solved to

$$N(t) = \frac{L}{R}(1 - e^{-Rt}) \tag{2.48}$$

with the initial conditions $N(T = 0) = 0$. The atom number increases and saturates at a maximum atom number

$$N_{\max} = \frac{L}{R}.$$

At higher densities, two-body collisions are clearly the dominant loss process in the MOT limiting its density. Solving equation 2.46 in the high density limit, the number of atoms is calculated to

$$N(t) = \frac{\sqrt{L^2 + 4R\beta'}}{2\beta'} \tanh\left(\frac{\sqrt{L^2 + 4R\beta'}t}{2\beta'} + \operatorname{arctanh}\left(\frac{L}{\sqrt{L^2 + 4R\beta'}}\right)\right) - \frac{L}{2\beta'} \tag{2.49}$$

When the atomic beam is blocked, i.e $L = 0$, the decay curve becomes

$$N(t) = N_0 \frac{Re^{-Rt}}{R + N_0\beta'(1 - e^{-Rt})}. \tag{2.50}$$

As already discussed in chapter 2.2.2, the loading rate L is predominantly determined by the properties of the Zeeman slower. But here are still some parameters left for optimisation that will be discussed in the next section.

Capture range and velocity

The ***capture range*** r_c is defined by the maximal distance an atom can have from the centre of the MOT so that it is still captured. The radius can be extracted from figure 2.9 to

$$r_{\mathrm{c}} = \frac{\hbar\delta_0}{\mu' \frac{\partial B}{\partial z}}. \tag{2.51}$$

An increase in capture radius allows lower densities, reducing the two-body losses in the MOT. Secondly, the solid angle of trappable atoms coming out of the oven is enlarged. This increases the loading rate of the setup. For a high maximum atom number in the MOT, r_{c} should be as large as possible.

Analogue, the MOT's ***capture velocity*** v_{c} is defined as the maximal atomic velocity still capturable. With a higher capture velocity v_{c}, a higher atomic flux can be achieved. This can be understood by considering following arguments:

1. With higher capture velocities of the MOT, higher end velocities for atoms leaving the Zeeman slower are allowed. Recalling equation 2.36 for the end velocity of the atoms after the slower

$$v_{\max} = \sqrt{v_{\mathrm{final}}^2 - 2aL}$$

shows, that the benefit of an increase in the end velocity is an increase of the slower's capture velocity. More atoms of the Boltzmann distribution can be slowed. In addition, the time of flight for the atoms from the end of the slower to the centre of the MOT is reduced. This decreases the loss of atoms due to the spread of the atomic beam (see section 2.2.2).

2. The MOT is able to recapture atoms which have gained kinetic energy via inelastic collisions. So the two-body loss factor can be decreased.

In summary, following parameters increase the capture performance of the MOT:

- Larger magnetic field gradients improve v_c.
- Larger detunings δ_{MOT} increase the r_c and v_c.
- Larger beams allow a larger capture volume. This plays an important role when r_c is limited by the size of the beams.

Temperature

The temperature of the MOT is expected to be in the same range as the temperatures in an optical molasses already discussed in chapter 2.1.3. Recalling the equation for the temperature of an optical molasses

$$k_B T = \frac{\hbar\gamma}{4}\frac{1+(2\delta/\gamma)^2}{|\delta|/\gamma},$$

one sees, that larger detunings lead to an increase in temperature. Lower temperatures are needed to transfer as many atoms as possible into the optical dipole trap. The optimisation of the temperature will be discussed in section 4.

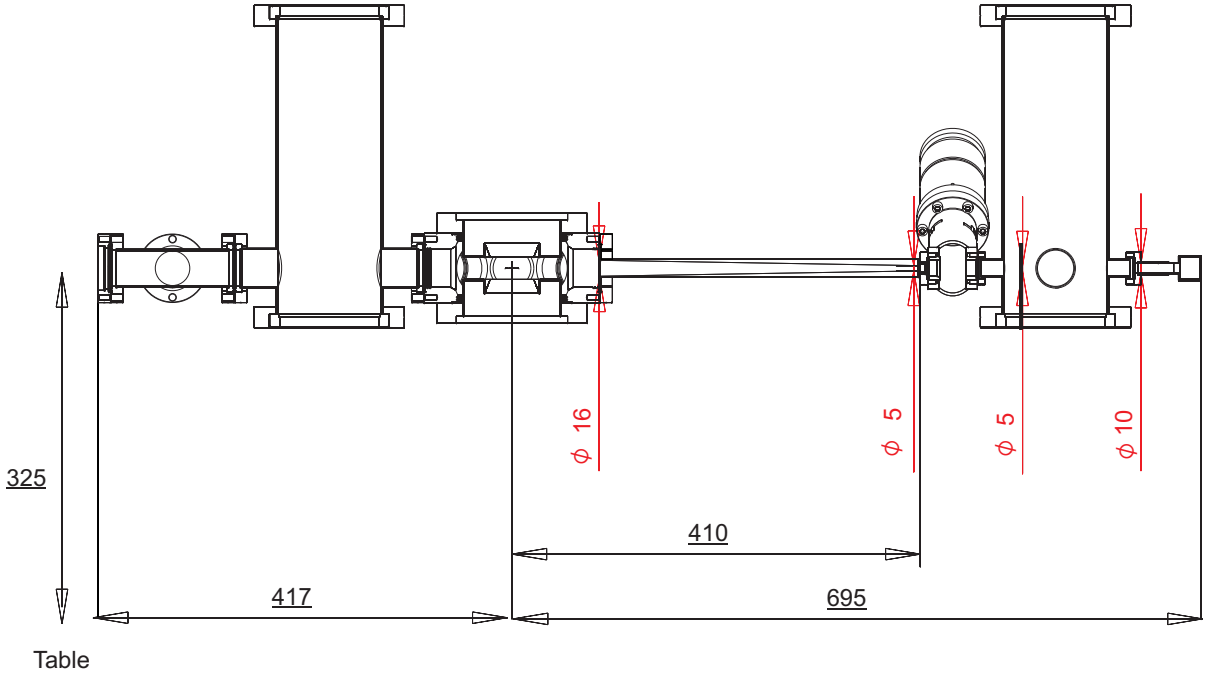

Figure 2.10.: *Dimensions of the complete setup. With $l \approx 1.2\,m$, the design is rather compact. By means of the gate valve between oven section and UHV chamber, the Lithium oven can be refilled without breaking the vacuum in the UHV chamber.*

3. Experimental setup

This chapter describes the vacuum system and setup for cooling and trapping. The following design goals have been realized within the experimental setup:

- **Ultra high vacuum in the trapping chamber**: The group of John Thomas demonstrated, that the storage time of neutral atoms in a far detuned dipole trap can be limited by collisions with background gas atoms [22]. In a system with few fermions, trap losses due to collisions are even more critical: Depending on the total number of atoms, the loss of one atom cannot be regarded as a small perturbation to the system. The energy levels of the whole system will change and the experimentator looses control over the system. Therefore, collisions with background gas atoms have to be suppressed as well as possible by means of a low background pressure on the order of $p \approx 10^{-12}$ mbar.

- **High repetition rate of the experimental cycle**: This characteristic is crucial for a fast optimisation of parameters later on. One bottleneck is the loading rate of the MOT which strongly depends on the atomic flux of trappable atoms provided by the oven and the Zeeman slower. A realistic aim for the loading rate are a few seconds.

- **Simplicity of the setup**: A simple layout is fast to set up, less error-prone, better to debug and has fewer parameters.

3.1. Vacuum system

The vacuum system should provide high atomic fluxes and an ultra high vacuum in the experimental chamber at the same time. This poses a challenge since the atomic flux is provided by an effusive Lithium oven heated up to 400 °C. The raising partial pressures of outgasing materials lead to an increasing pressure in the system. To overcome this problem, the vacuum system, as shown in figure 3.1, has been divided into two main parts:

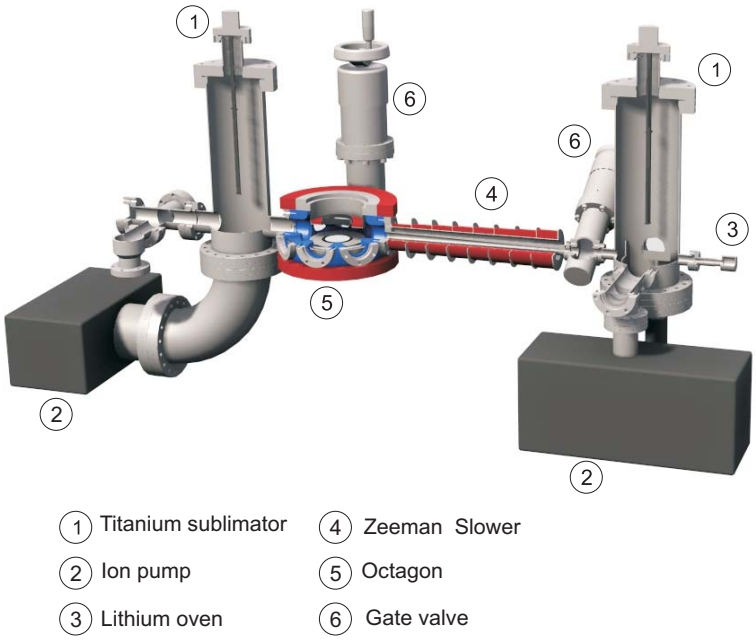

Figure 3.1.: *Complete vacuum system.*

1. **Oven chamber**: Contains the heated lithium oven, therefore operates at higher pressures $p \approx 10^{-10}$ mbar.

2. **Experimental chamber**: UHV chamber where experiments are performed.

A differential pumping section with low conductance l between the two chambers is needed to maintain the desired pressure ratio between oven chamber and experimental chamber. The differential pumping section is realized with a 300 mm long conical tube opening up from

$$r_{\text{in}} = 2.5\,\text{mm}$$

to

$$r_{\text{out}} = 8\,\text{mm}$$

corresponding to a capture radius of the MOT

$$r_{\text{MOT}} \approx 11\,\text{mm}.$$

This value was chosen to be a bit smaller than the diameter of 1" MOT beams. With the value for $r_{\text{in}} = 2.5\,\text{mm}$ and the average velocity

$$\overline{v} = \sqrt{\frac{8k_BT}{\pi m}},$$

a conductance

$$l = \frac{\pi r_{\text{in}}^2 \overline{v}}{4} \frac{1}{(1 + \frac{r_{\text{in}}+r_{\text{out}}}{4r_{\text{out}}^2} l)} \approx 0.7\,\text{l/s}$$

can be obtained [19].

The pressure aimed on the oven side

$$p_{\text{oven}} \approx 10^{-10}\,\text{mbar}$$

is a realistic value as it can be seen in section 3.1.1. The pumping speed needed for a final vacuum in the experimental chamber

$$p_{\text{exp}} \approx 10^{-12}\,\text{mbar}$$

can be estimated to

$$S_{\text{exp}} \approx l \cdot \frac{p_{\text{exp}}}{p_{\text{oven}}} \approx 70\text{l/s}.$$

As shown in the next section, this is also a realistic number for our experiment.

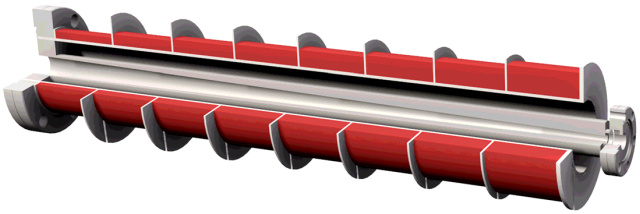

Figure 3.2.: *Zeeman slower mounted on differential pumping tube. A CF40 flange (left) connects the differential pumping section to the experimental chamber. A groove within the flange supplies a mount for the aluminium tube of the Zeeman slower. The tube is just large enough to fit over the CF16 flange (right) leading to the oven section. A short bellow inserted into the CF16 flange provides the flexibility needed for the assembly.*

The conical tube is connected to the experimental chamber with a machined CF40 flange. A groove in the flange provides a simple mount for the aluminium

tube of the Zeeman slower as shown in figure 3.2. Towards the oven chamber, a short bellow of a few millimetres has been inserted into the CF16 flange. By that means small deviations in the angle due to construction and assembly can be compensated.

We set the hole in the CF16 flange for the atomic beam not in the centre of the flange, but shifted it 0.5 mm downwards since the height of the additional aperture in front of the Zeeman slower tube was 0.5 mm too low. One reason for this discrepancy could be an accumulation of deviations still lying within the tolerances of the individual parts. The all metal gate valve (VAT) between the two sections has been inserted for two reasons:

1. The Lithium oven can be refilled without breaking the vacuum in the experimental chamber.

2. To obtain the UHV in the experimental chamber, the conductance of the differential pumping tube can be defined by chosing an appropriate diameter after one has made sure that the desired vacuum in the oven section can be reached.

For maintaining an UHV, low outgasing rates of the parts in the vacuum chamber are essential. The gate valve was chosen all metal, because its outgasing rate is small compared to a (cheaper) valve containing viton gaskets.

3.1.1. The oven chamber

Vacuum

A high vacuum requires high pumping speeds for all gases. For that reason, the vacuum in the oven chamber is maintained by means of a combination of two pumps:

1. A titanium sublimation pump (TSP) (VARIAN) connected to a 6-way CF100 cross (TRINOS, custom made) is used to pump all reactive gases like H_2. The TSP coats nearly the whole surface of the CF100 cross with titanium. In a chemical reaction, gases can be gettered into the surface, so the pumping speed of a TSP is proportional to the surface used. As listed in table 3.1, typical values for the pumping speed of the surface used in our experiment $A \approx 1000\,\mathrm{cm}^2$ reach up to $S = 3100\,\mathrm{l/s}$ for H_2.

2. Non-reactive gases, especially noble gases, can be pumped with an ion pump (VARIAN StarCell 40 l/s for H_2,15 l/s for Ar, CF40). Compared

	H_2	O_2
typical pumping speed [l/(s cm^2)]	3.1	9.3

Table 3.1.: *Pumping speeds of a titanium sublimation pump. The pumping speed is proportional to the area coated with titanium. The more reactive the gases are, the more efficient they can be pumped by the titanium film. The values are taken from the VARIAN website and valid for a temperature of $T = 20$ ℃.*

to other ion pumps, the StarCell model reaches lower pumping speeds for H_2, but explicitly high pumping speeds for noble gases like Argon.

The height of the atomic beam is defined by the height of the two CF16 flanges and set to

$$h = 60\,\mathrm{mm}$$

measured from one end of the CF100 tube. A TSP has to be placed such that nearby viewports are not coated with titanium. To protect the two CF40 viewports from the emission angle of the TSP, the length of the cross is set to

$$l = 300\,\mathrm{mm}.$$

A conservative estimation for the combined pumping speed of both pumps for H_2 adds up to

$$S_{\mathrm{oven}} \approx 200\,\mathrm{l/s}.$$

This means for an aimed vacuum of

$$p_{\mathrm{oven}} \approx 10^{-10}\,\mathrm{mbar}$$

a leak rate of

$$Q_{\mathrm{leak}} = S_{\mathrm{oven}} \cdot p_{\mathrm{oven}} \approx 2 \cdot 10^{-8} \frac{\mathrm{mbar\,l}}{\mathrm{s}}$$

is acceptable. The leak rate is dominated by the partial pressures of the outgasing materials in the oven filled with Lithium. It has been known from previous experimental experience that this rate is lower than the pumpable leaking rate.

When the oven is heated, the final vacuum reaches

$$p_{\mathrm{oven}} \approx 10^{-10}\,\mathrm{mbar}.$$

Effusive lithium oven

One of the most important parts of the experimental setup is the effusive Lithium oven:

- **High atomic flux** is provided by the rather large aperture $r = 5\,\text{mm}$ of the oven. At $T_{\text{oven}} \approx 400\,°\text{C}$, the aperture enables an atomic flux of

$$f = \frac{n\overline{v}}{4\pi r^2} \approx 4 \cdot 10^{16}\,\frac{\text{atoms}}{\text{s}}.$$

- **UHV vacuum** in the experimental chamber requires a vacuum of

$$p \approx 10^{-10}\,\text{mbar}$$

  in the oven section. Since this pressure is limited by outgasing materials in the oven, the large aperture of the oven has a high conductance and therefore allows very efficient pumping of all gases during the bakeout of the chamber. By this means, the outgasing rate after the bakeout can be reduced to a minimum.

The oven's capacity of 0.6 g ≙ $1\,\text{cm}^3$ of Lithium should ensure about 2500 hours of operation at $T_{\text{oven}} \approx 400\,°\text{C}$.

The emission angle is merely defined by the oven's dimensions to

$$\tan\alpha = \frac{d}{l} = \frac{10\,\text{mm}}{45\,mm}$$

leading to

$$\alpha \approx 12°.$$

As shown in figure 2.10, an additional aperture with a diameter of $d = 5\,\text{mm}$ is needed in order to prevent the lithium atoms from coating the valve. The sharp edges of the coated area on the plate of the aperture confirm the estimated beam divergence experimentally.

Atomic beam shutter

A beam shutter consisting of a rotatable, stainless steel plate polished on both sides serves for three purposes, depending on its orientation (see figure 3.3:

1. Blocking the atomic beam.
2. Enabling the view into the Lithium oven.

3. Adjustment of the position and power of the Zeeman slower laser beam through one of the CF40 flanges. For that reason, we measured the plate's reflection coefficient to

$$R \approx 0.5 \,\text{at}\, \lambda = 671\,\text{nm}.$$

Figure 3.3.: *Atomic beam shutter. Depending on its orientation, it can not only be used for blocking the atomic beam. By using it as a mirror, it provides views into the oven. In addition, the Zeeman slower laser beamed can be aligned from outside the chamber.*

The beam shutter is connected to a rotatable vacuum feedthrough (MDC) which can be controlled electronically via a servo motor. The time between open/close position does not exceed 0.5 s. When the atomic beam is blocked,

one side of the shutter gets coated with Lithium which destroys its reflectivity. This is not a serious problem since the other side can still be used for viewing. For the technical drawing, see A.8. Another possibility to clear the coated mirror plate again is to evaporate the Lithium coating with a fibre laser: the absorption coefficient of the mirror for a wavelength $\lambda = 1070\,\mathrm{nm}$ is roughly $20\,\%$. So with the 200 Watt fibre laser, one can deposit a large amount of heat in the mirror, leading to an evaporation of the lithium coating.

3.1.2. The experimental chamber

Geometry

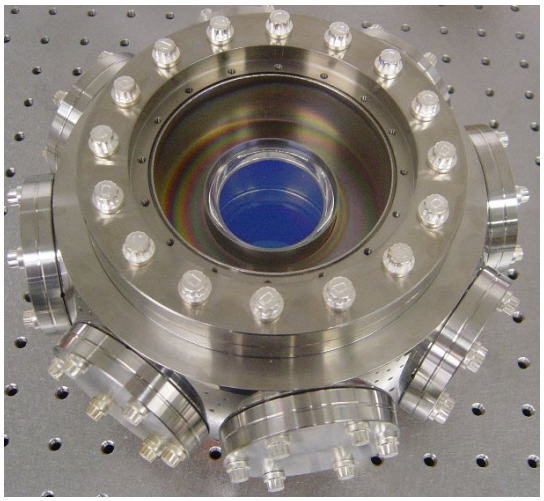

Figure 3.4.: *Octagon with reentrant viewports. On the one hand, they provide optical access under a large solid angle. This allows a high numerical aperture* $NA \approx 0.65$ *for detection of the atoms and for focusing the microtrap beam to a waist* $w_0 \approx 1\,\mu m$*. One the other hand, the reentrant windows provide a mounting for the Feshbach coils to bring them together as close as possible. By that means, the power needed for the high magnetic fields is minimised.*

In the following, the two basic prerequisites on the experimental chamber for an experiment with few ultracold atoms are discussed:

1. The main tools for the preparation and manipulation of samples of ultracold atoms are lasers. Thus, the chamber has to provide ***plenty of optical access***. A spherical octagon (KIMBALLPHSICS) suites our

needs with 8 CF40 flanges and two CF100 flanges providing access from all directions. In addition, one more issue has to be taken into account for the preparation of a mesoscopic sample of fermions: A small waist $w_0 \approx 1\,\mu$m of the dipole trap is needed to keep the number of allowed states small. On the other hand, the detection signal of photons emitted by few atoms is very weak, so a ***large solid angle*** of detectable photons is crucial. To obtain both a minimised waist w_0 and a maximised solid angle, a lens with high numerical aperture will be used. To keep flexibility, the lens will be mounted outside the chamber. So the numerical aperture is limited by the geometry of the viewports. For that reason, two CF100 custom made reentrant viewports (special techniques group of the UKAEA) have been designed as shown in figure 3.4: They supply a viewing angle through the windows into the octagon of

$$\theta \lesssim 45^\circ$$

and enable a numerical aperture of

$$NA \approx 0.65.$$

2. A further point to be considered are the ***high magnetic fields*** needed for tuning the scattering length: The Feshbach coils should be able to supply up to 1500 Gauss. The larger the distance between the pair of coils, the larger is the amount of produced heat. The reentrant viewports solve this problem since they provide a mount for the Feshbach coils as shown in figure 3.5.

   Thus, it is possible to reduce the distance between the pair of coils to

   $$d_{\text{Feshbach}} = 31\,\text{mm},$$

   so the power needed for the rather high magnetic fields is mangageable. Details on the Feshbach coils are given in chapter 3.2.3.

Vacuum

The vacuum in the experimental chamber is maintained by means of the same combination of pumps used in the oven section: An ion pump (VARIAN StarCell Vaclon Plus75, 20 l/s for Ar) together with a titanium sublimation pump (VARIAN) in a CF100 tube reach pumping speeds from 100-1000 l/s. In spite of

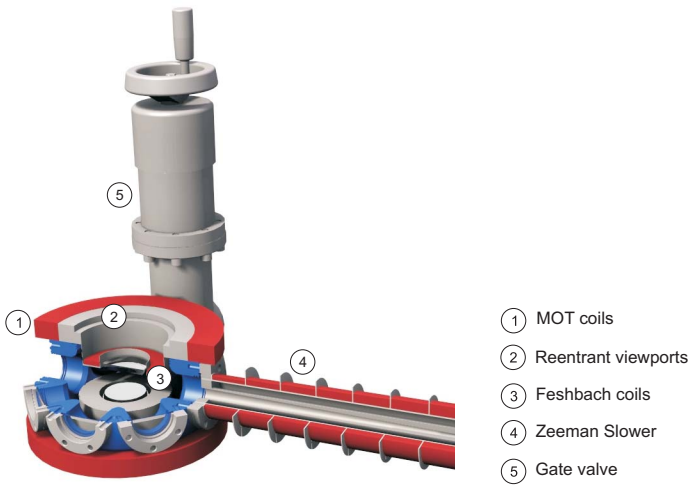

Figure 3.5.: *The experimental chamber. The reentrant viewports provide not only optical access but also a mount for the two different pair of coils creating the Feshbach fields and the fields for the Magneto Optical Trap. The gate valve can be used for introducing detection and manipulation tools into the experimental chamber without breaking the vacuum.*

the high pumping speeds, the vacuum in the octagon is limited by the conductance of the CF40 tube. Thus, a third pumping technique is used in addition to the two conventional pumps: The walls of the octagon have been coated with a NEG (Non Evaporable Getter coating) at GSI [23]. Developed at CERN, the TiZrV alloy prevents not only outgasing of the underlying substrate, but also pumps similar to a titanium sublimation pump residual gas molecules. Its pumping speed reaches $0.5\,\mathrm{l/(s\,cm^2)}$ for H_2. The coating gets activated after 24 h at 180 °C and can be reactivated several times.

It has some striking advantages over a titanium sublimation pump:

1. No extra space has to be used and the pumping happens directly where it is needed. Therefore, the pumping speed is not limited by the conductance of a CF40 connecting tube.

2. The coating can be applied *before* the system gets evacuated. So surfaces inaccessible for titanium sublimation pumps can be used for pumping.

In our case, almost the whole surface of the octagon is used for pumping directly the experimental chamber.

With those three pumps, a vacuum on the order of

$$p \approx 10^{-12}\,\mathrm{mbar}$$

is reached experimentally.

Flexibility

To have the possibility to upgrade the trapping chamber later without breaking the vacuum, a CF40 gate valve (VAT) is connected to the octagon via a closed coupler (KIMBALLPHSICS). One possible application could be a multi channel plate for ionisation imaging of the atoms.

3.2. Cooling and trapping setup

A Zeeman slower is used to precool as many atoms as possible out of the atomic beam to velocities smaller than the MOT's capture velocity. In the following chapter the final design of Zeeman slower and MOT as well as the laser system will be discussed.

3.2.1. Laser system

Our requirements on the laser system for an experiment with ultracold lithium atoms are the following:

1. For laser cooling, the bandwidth of the laser has to be small compared to the natural linewidth of Lithium $\gamma/2\,\pi = 5,87\,\mathrm{MHz}$.

2. The frequency stabilisation should be implementable with a rather simple scheme. For imaging in high fields, it should be tunable over a range of $1 - 2\,\mathrm{GHz}$.

3. Sufficiently high output powers should be available at comparable low costs.

For those reasons, our choice is a diode laser system from (TOPTICA) consisting of:

- Two single mode diode lasers with output powers of 20 mW each
- One tapered amplifier (TA) with an output power of 500 mW.

Figure 3.10 represents a sketch of the laser system. One of the diode lasers is used as a reference laser. Its grating forms a resonator with the back side of the diode and can be adjusted via a piezo. A coarse selection of the wavelength can be done by turning the grating, the finetuning of the frequency is realized by moving the grating back and forth. This changes the length of the cavity and thus the frequency ω_{ref}. To stabilise the reference laser on an atomic transition, a signal controlling the piezo, called feedback signal, has to be generated. The method of Doppler-free RF-spectroscopy is used since the atomic hyperfine structure can be resolved, which is needed for laser cooling.

The laser frequency ω_{ref} is modulated with a radio frequency ω_{RF} leading to a carrier frequency ω_{ref} and mainly two sidebands at frequencies

$$\omega_{\pm} = \omega_{\mathrm{ref}} \pm \omega_{\mathrm{RF}}.$$

This can be realized by modulating the current on the laser diode with a voltage controlled oscillator (VCO). The light passes a spectroscopy cell filled with Lithium, is retro reflected to cancel out the atom's Doppler shift and is finally recorded with a fast photodiode. To get information about ω_{ref} with respect to an arbitrary transition ω_0 of Lithium, the idea is to observe the difference in transmission

$$\Delta T = T_+ - T_-$$

and phase shift

$$\Delta\psi = (\psi_+ - \psi_{\mathrm{ref}}) + (\psi_- - \psi_{\mathrm{ref}})$$

of the two sidebands in the spectroscopy cell.

If e.g.

1. $\Delta T = 0$, the two sidebands experience the same absorption meaning $\omega_{\mathrm{ref}} = \omega_0$
2. $\Delta T > 0$, the absorption for sideband $\omega_{\mathrm{ref}} - \omega_{\mathrm{RF}}$ is stronger so $\omega_{\mathrm{ref}} > \omega_0$
3. $\Delta T < 0$, the absorption for sideband $\omega_{\mathrm{ref}} + \omega_{\mathrm{RF}}$ is stronger so $\omega_{\mathrm{ref}} < \omega_0$

For that reason, a signal depending on ΔT and $\Delta\psi$ is needed and can be prepared in the following way: With a modulation amplitude M and a transmission coefficient T_0 for the carrier frequency ω_{ref}, the signal on the photodiode is given by

$$U_{\mathrm{PD}} \propto T_0^2 + MT_0\Delta T \cos\omega_{\mathrm{RF}}t + MT_0^2\Delta\psi \sin\omega_{\mathrm{RF}}t$$

[20].

The signal of the photodiode is demodulated with ω_{RF} again and higher frequency components are cut out with a low-pass filter. The final final signal now depends on the desired parameters:

$$U_{\mathrm{final}} \propto \Delta T \cos\phi - \Delta\psi \sin\phi.$$

The phase shift ϕ between the modulated signal before the spectroscopy cell and the demodulated signal after the spectroscopy cell can be adjusted via a tunable delay of the VCO. So the dependence of the signal can be smoothly tuned from pure absorption to pure dispersion of the sidebands. For small deviations $\omega_{\mathrm{ref}} - \omega_0$ the signal is proportional to $\omega_{\mathrm{ref}} - \omega_0$.

The power for the MOT beams and the Zeeman slower beam is provided by the tapered amplifier. Its frequency is stabilised relative to the frequency of the reference laser. The idea of the stabilisation follows the paper of Zielonkowski et al. [13]: The light of the reference laser and the tapered amplifier are overlapped and their beating signal

$$\Delta\omega = \omega_{\mathrm{TA}} - \omega_{\mathrm{ref}}$$

is recorded with an amplifying photo diode. Then, the beating signal is mixed with the output of an VCO producing a sum and a difference frequency of the beat and the VCO

$$\Delta\omega \pm \omega_{\mathrm{vco}}.$$

The signal is split into two equal parts. After delaying one part with a $2\,m$ coax cable, the signals are mixed again in a phase detector. Since only the difference frequency $\Delta\omega - \omega_{\mathrm{vco}}$ is used, the sum frequency is suppressed via a low-pass filter. The phase shift

$$\Phi = (\Delta\omega - \Delta\omega_{\mathrm{vco}})\tau$$

between the two signals introduced by the cable gives rise to an output signal

$$U \propto \cos\Phi.$$

A zero crossing of the signal can be used as error signal for adjusting the frequency ω_{TA} via the diode laser's grating.

As described in section 2.2, the hyperfine splitting of the ground state demands two frequencies for keeping the atoms in the cooling cycle: the repumping and the cooling transition. So the light of the tapered amplifier is split into two parts. The cooler frequency is shifted $\Delta\nu = -114\,\mathrm{MHz}$ whereas the

repumper is shifted $\Delta\nu = +114\,\mathrm{MHz}$ via two acousto optic modulators (AOMs) corresponding to the hyperfine splitting

$$\Delta E/h = 228\,\mathrm{MHz}$$

of the ground state of ^{6}Li. The two beams are superposed again such that the resulting beam contains both frequencies. Afterwards, it is subsequently divided into four beams: three MOT beams and one beam for the Zeeman slower.

The light for the Zeeman slower has to be shifted another few linewidths with a third AOM. All of the beams are then coupled into fibres for three reasons:

1. **Beam profile**: The beam profile is clean after the fibre with a nearly perfect gaussian intensity distribution.
2. **Space**: A fibre outcoupler combined with an intergrated $\lambda/4$ plate for circular polarisation only occupies a small part of the rare space near the experimental chamber.
3. **Alignment**: The fibre outcouplers are easy to align since only three degrees of freedom have to be adjusted.
4. **Flexibility**: The complete laser system can be built up on an additional table.

So the advantages of fibres outweigh the disadvantage of loosing 30-40 % of the total laser power. After the fibres, the 3 MOT beams are retro reflected to confine the atoms in three dimensions.

Experimental values for the laser intensities after the fibres are listed in table 3.2

	Cooler mW/cm^2	Repumper mW/cm^2
MOT beams (incl. retro reflected)	36	18
Zeeman slower beam	10	5

Table 3.2.: *Available laser intensities. The laser intensities in the MOT reach* $\approx 20 \cdot s_0$*, so the atomic scattering rate is expected to be close to the on resonance scattering rate* $\gamma/2$*.*

The second diode laser is needed for absorption and fluorescence detection of the atoms. Therefore, a beat offset lock with respect to the reference laser is

planned. Since the detection should be possible in high magnetic fields up to 1500 Gauss, its tunability should be in the range of

$$\Delta\omega \approx 1 - 2\,\mathrm{GHz}.$$

3.2.2. Zeeman slower

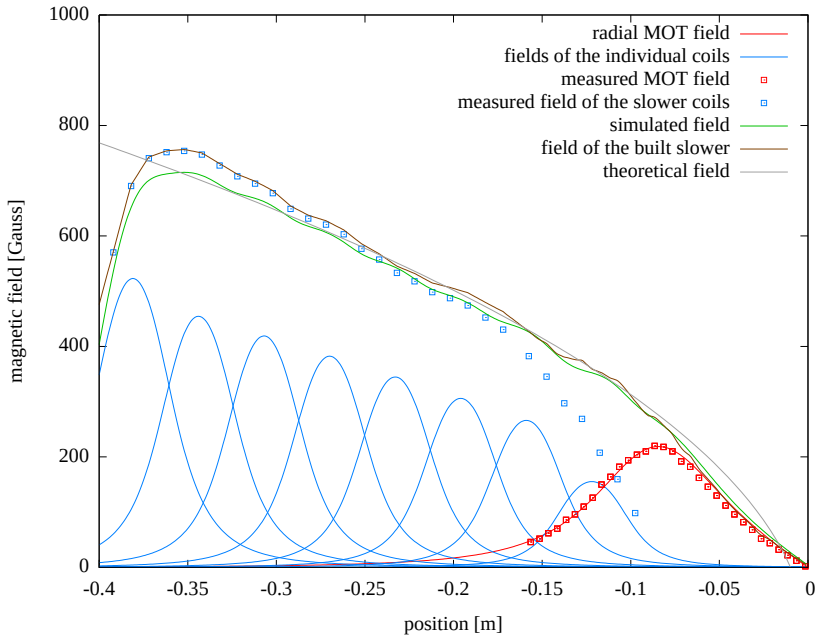

Figure 3.6.: *Simulated and measured magnetic fields of the Zeman slower. Zero position indicates the centre of the MOT. To minimise the atom's time of flight before they reach the capture radius of the MOT, the last part of the Zeeman slower field is created by the radial MOT field. Both the simulated and the measured fields are smooth over the whole range and show good agreement with the theoretical field. At the beginning, the field of the built Zeeman slower is larger than the theoretical field providing a higher capture velocity of* $v_c \approx 800$ *m/s.*

The important design parameters have already been discussed in chapter 2.2.2. Calculations of the magnetic fields were performed with a modified version of a MATHEMATICA notebook from John Thomas' group [24]. An increase in atomic flux of a factor of three can be archieved, when the slower is able to decelerate all of the three possible hyperfine states shown in figure

2.5. Therefore the optimum slope of the field was determined in an iterative process:

1. The slope of the theoretical field for a decreasing field configuration was calculated neglecting the atom's hyperfine structure of the Zeeman effect. This approximation is only reasonable in the high field regime as seen in chapter 2.2. The field of a virtual slower consisting of 8 coils was calculated such that the deviations from the theoretical field were as small as possible.

2. The resulting magnetic field was imported into a MATLAB simulation, where the atom's effective detuning during the deceleration was calculated at each timestep. For that purpose, the exact Zeeman shifts of the ground state including the magnetic hyperfine sublevels were calculated via the Breit-Rabi-Formula.

3. In the case of too large effective detunings at certain sections of the magnetic field, the atom could not be decelerated further. In this case, the magnetic field was adapted and simulated again.

The iteration finished when the calculated magnetic field could decelerate all three hyperfine states in the simulation. The most critical part of the magnetic field turned out to be the section where the field of the 8th coil is merged with the radial MOT field. To provide a smooth overlap of the fields, the 8th coil is powered individually. Table 3.3 gives an overview over the final parameters chosen for the Zeeman slower. The setup consists of 8 individual magnetic coils. On the one hand, this minimises the damage in case of a short circuit, on the other hand it provides the flexibility to vary the current in the individual coils. For coils $1-7$, the same currents

$$I_{1-7} = 6.4\,\mathrm{A}$$

are planned, coil 8 gets

$$I_8 = 5.6\,\mathrm{A}.$$

The windings for the coils can be taken from table 3.4 The magnetic fields measured with a hall sensor are plotted against the position in figure 3.6. The agreement between calculated magnetic field (blue) and simulated field (green) is good over almost the whole range.

The holder for the coils is provided by an aluminium tube machined on a lathe. 8 grooves were cut into the aluminium tube to serve as a mount for the

configuration	decreasing field
length	40 cm including MOT field
coils	8
current coil $1-7$	$6,5$ A
current coil 8	$5,6$ A
max magnetic field	754 Gauss
maximum capture velocity	800 m/s
expected flux	$\approx 10^{11} \frac{\text{atoms}}{\text{s}}$
detuning	-125 MHz
total power	370 W
saturation parameter s/s_0	4

Table 3.3.: *Parameters of the Zeeman slower. 8 individual coils provide the flexibility to overlap the Zeeman slower field with the radial MOT field smoothly.*

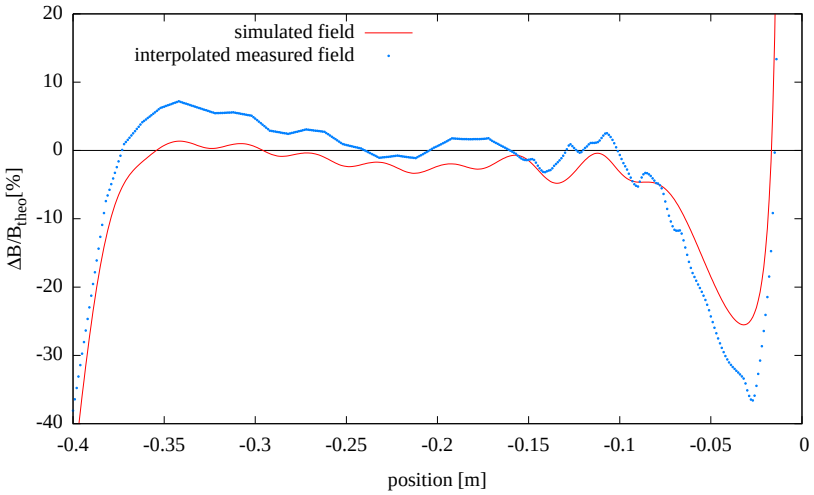

Figure 3.7.: *Relative deviation of simulated and measured magnetic fields from the theoretical field. Zero position indicates the centre of the MOT. The atoms are on resonance within a long area of deceleration: From $z \approx -37$ cm to $z \approx -6$ cm, the relative deviations are smaller than 10%. The larger deviations near the MOT centre result from the gradient of the linear radial MOT field. Simulations show that the atoms are still enough resonant in the area $z > -6$ cm so that they can be decelerated up to $z \approx 1$ cm. With an end velocity $v_{\text{end}} \approx 60$ m/s, they are slow enough to be captured by the MOT.*

coil	windings in simulation	real windings	deviation (%)
1	128	125	-2.3
2	192	194	+1
3	224	224	0
4	256	244	-4.7
5	288	283	-0.3
6	320	321	+0.3
7	352	363	+3.1
8	416	416	0

Table 3.4.: *Windings for the simulated and the built Zeeman slower. Reaching the exact number of windings was difficult in practice. Nevertheless, the deviations from the simulated windings are smaller than 5%. This was confirmed by the good results in the simulation of the measured field.*

coils. Between two grooves, a 1 mm thick spacer has been left over to enable a homogeneous winding. The inner diameter of the aluminium tube

$$d_{\text{in}} = 35\,\text{mm}$$

is just large enough so that the tube fits over the CF16 flange of the differential pumping tube. Because of the rather large amount of heat produced by the slower, $P \approx 370\,\text{W}$, a water cooling system is connected to 8 of the spacers. Details on the water cooling system can be found in the appendix (figure A.2). With the water cooling running, the temperature of the coil producing the highest field amounts to 100 ℃.

3.2.3. Magneto optical trap and Feshbach fields

MOT

As figure 3.5 shows, the coils for the MOT are wound around the CF100 flanges of the reentrant viewports. The distance between the two coils is just large enough to provide a radial magnetic field which extends to the end of the Zeeman slower. By that means an optimum overlap betwen the field of the Zeeman slower and the radial MOT field can be found.

The properties of the coils producing the MOT fields are listed in table 3.5.

The calculated radial and axial magnetic fields are plotted in figure 3.8 The water cooling of the MOT coils is realized with a copper plate flooded with

$B_{\max}$	200 Gauss
wire dimensions	5 x 1 mm
windings axial	4
windings radial	24
current	32 A
total power each coil	200 W

Table 3.5.: *Properties of the coils producing the fields for the MOT. The dimensions of the flat wire are chosen such that both a high fill factor copper/area and a simple layout can be realized: 4 windings in axial direction just fit over the CF100 flange of the reentrant viewports.*

water on top of each coil. Details on the water cooling system can be found in the appendix A.1.

Feshbach fields

The fields for tuning the atomic scattering length are created with a pair of coils in Helmholtz configuration. Their design is more challenging than the setup of the MOT fields, because the requirements differ:

- The coils have to produce high fields up to 1500 Gauss to tune the scattering length over a wide range.
- The fields has to be as homogeneous as possible to ensure a homogeneous scattering rate within the atomic sample.
- The layout has to be as simple as possible and has to operate at a minimum of power.

The appropriate wire dimensions play a key role: To ensure a homogeneous field, an exact Helmholtz configuration is needed. That means the dimensions of the wire have to be chosen such that they support the Helmholtz configuration as well as possible. At the same time, the fillfactor

$$f = \frac{\text{amount of copper}}{\text{total cross section}}$$

of the wire has to be as large as possible to minimise the power produced. A flat wire with a large aspect ratio meets the requirements best. For our setup,

[h!]

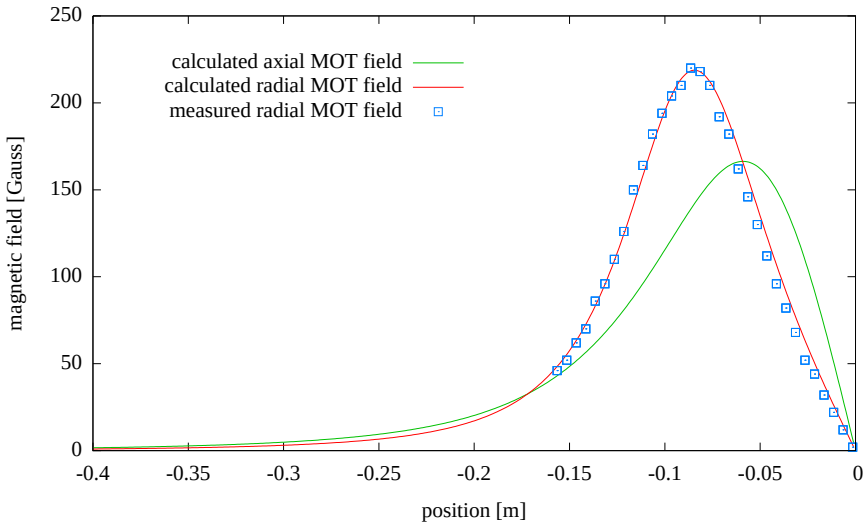

Figure 3.8.: *Calculated axial and radial MOT fields. Zero position indicates the centre of the MOT. The measured field is consitent with the calculations. A radial magnetic field gradient of* $\frac{\partial B}{\partial z} = 20\,Gauss/cm$ *is needed to overlap the fields of the Zeeman slower and the MOT.*

$B_{\max}$	$\approx 1500\,\text{Gauss}$
wire dimensions	5x1 mm
windings	15
maximum current	400 A
total power per coil	$\approx 2000\,\text{W}$
max amount of heat per area	44W/cm^2
Pentium 4 Prescott	61W/cm^2

Table 3.6.: *Properties of the Feshbach coils. The high magnetic fields lead to an enormous amount of produced heat. The maximum amount of heat/cm*^{2} *reaches the same order of magnitude as a Pentium 4 Prescott.*

we use a 1 mm thick wire with the largest aspect ratio available: 5x1 mm. Table 3.6 gives details on the planned magnetic fields.

The calculated magnetic fields are plotted in figure 3.9. In spite of the small distance between the coils and the large fillfactor, the amount of heat produced by one coil adds up to 2000 W. Thus a simple cooling system is being tested at the moment. Similar to the cooling of the MOT coils, it will be realized with a

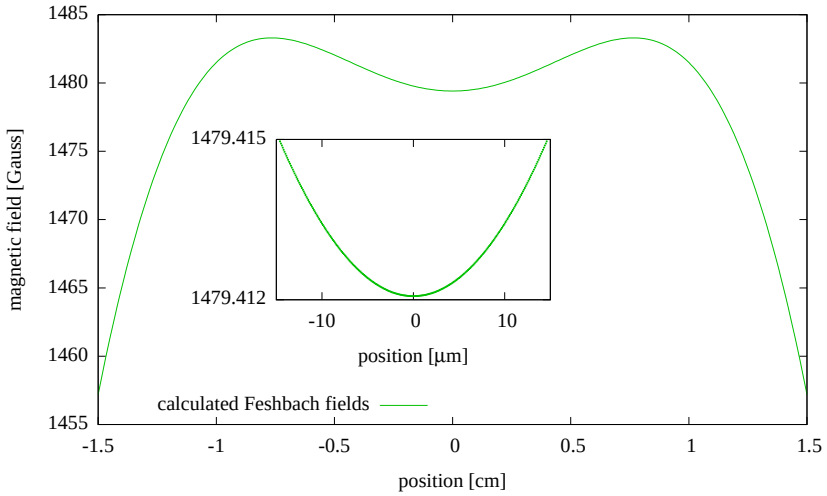

Figure 3.9.: *Planned fields for tuning the scattering range. To tune the atomic scattering length over a wide range, the magnetic fields have to be as large as* $B_{\max} \approx 1500$ *Gauss. They also have to be as homogeneous as possible to enable homogeneous atom interactions. Therefore, the dimensions of the wire have to be such that an exact Helmholtz configuration is reached within the coils. With wire dimensions of* $5\,x\,1$ *mm, the magnetic field only varies within a range of a few mGauss over the trap size of a few micrometer. The current needed to produce such high fields is minimised by the short dimensions of the coils, but still amounts to* $I = 400\,A$.

water flooded copper ring glued on top of each coil. The system works well for $I = 200$ A in continuously operation and has some reserves for up to $I = 350$ A for short times.

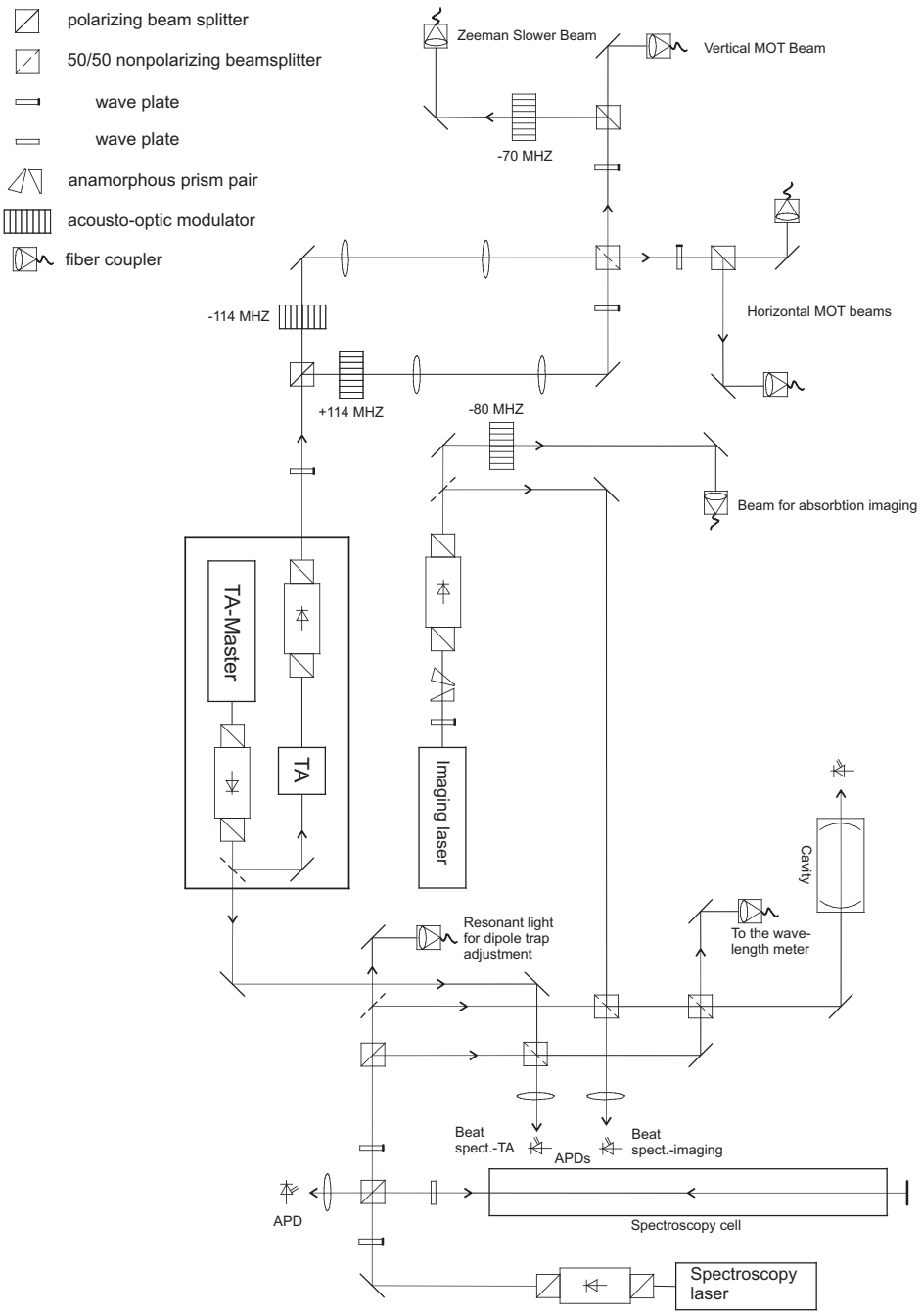

Figure 3.10.: *Complete laser system. Drawing: Thomas Lompe.*

4. Properties of the magneto optical trap

The characteristics of our MOT are described in this chapter. A good overlap between the cold atomic cloud and the volume of the optical dipole trap is needed to transfer as many atoms as possible into the dipole trap. For that reason, the loading procedure is performed within two stages:

1. ***Loading stage***: Parameters are optimised to collect a high total number of atoms. Especially large detunings allow many atoms in the trap (see 2.2.3).

2. ***Compression stage***: For a good overlap with the dipole trap and low temperatures, the atomic cloud is compressed by decreasing the detuning: At small values for the detuning, higher number densities can be reached and the temperature decreases (see also section 2.2.3) leading an increase in phase space density. As a rule of thumb, the kinetic energy of an atom within the cloud should not be larger than $E_{kin} \approx \frac{1}{10} U_{dipole}$ where U_{dipole} is the depth of the optical dipole trap.

In the following, the tools necessary for detection are described. Furthermore, measurements of the atom number and temperature are reported.

Computer control

To time events on a microsecond timescale, a realtime computer control system (ADwin) is used. It provides 8 analogue outputs and 32 digital channels that can be used both as as in- and outputs. At the moment, the channels are used to control following devices:

1. Laser beam shutters (digital out)

2. Atomic beam shutter (digital out)

chip size (binned)	375x240 pixel
pixel size	8.4 x 9.8 μm
effective pixel size after binning	16.8 x 19.6 μm
minimum exposure time	50 μs
resolution depth	8 Bit

Table 4.1.: *Properties of the Guppy F-038 B NIR CDD camera. At comparable low costs, the camera's sensitivity is high enough to take fluorescence images of the atomic cloud.*

3. Detuning of the MOT beams via the input voltage for the VCO of the beat offset lock (analog out)
4. Intensities of MOT and Zeeman slower beams via a variable attenuator before the RF input of the AOMs (analog out)
5. Camera trigger (digital out)
6. Magnetic fields of the Zeeman slower (digital out)

Detection system

For the characterisation of the MOT, the fluorescence light of the atom was detected. For this kind of measurement, the requirements on a camera are as follows:

1. High sensitivity at $\lambda = 671\,\text{nm}$ to detect small fluorescence signals
2. Short exposure times to resolve dynamics of the atomic cloud

The camera used for this purpose is a GUPPY F-038 B NIR (AVT) with specifications listed in table 4.1.

The camera is placed in front of a CF40 viewport of the experimental chamber. To project an image of the atomic cloud with a diameter $d \approx 1$mm onto the camera's CCD chip, the picture has to be scaled down. Therefore the collected light passes a telescope setup of two standard lenses ($f_1 = 150\,\text{mm}$, $f_2 = 60\,\text{mm}$), providing a scale factor of f_1/f_2=2.5 before it is detected with the CCD chip. To eliminate noise coming from stray light, a background offset is subtracted from each image. The offset is calculated from the average pixelsum of ten dark ground images. To image the atomic cloud with a delay as short as

possible, the camera is triggered electronically via our ADwin computer control system. After having a trigger event, the camera has a short delay of 10 μs before the picture is taken.

Calibration

For the determination of the atom number, the counts on the camera have to be calibrated to the number of photons emitted from the atomic cloud. Therefore, the following fact has to be taken into account: The camera covers only a fraction

$$\Omega = \frac{r_{\text{aperture}}^2 \pi}{4\pi d_{\text{lens}}^2} \approx (4 \pm 0.8) \cdot 10^{-4}$$

of the solid angle of emitted photons. The large error is due to the fact, that both the radius of the aperture $r = (6 \pm 0.5)$mm and the distance of the first lens to the atoms $d_{\text{lens}} = (150 \pm 5)$mm are not known more precisely. To determine the number of emitted photons per count, the camera's CCD chip is illuminated with a light source of known power P for a known period of time t_{exposure}. The number of **emitted** photons is then given by

$$N_{\text{photons}} = \frac{1}{\Omega} \frac{P t_{\text{exposure}}}{\hbar \omega}.$$

Exposing for $t_{\text{exposure}} = 250\,\mu$s, one gets 43000 counts leading to a a conversion factor

$$\eta_{\text{photons}} \approx \frac{1}{4 \cdot 10^{-4}} \frac{7.7 \cdot 10^6}{43000} \frac{\text{photons}}{\text{counts}} \approx (4.5 \pm 0.9) \cdot 10^5 \frac{\text{photons}}{\text{count}}.$$

η_{photons} is a property of the camera settings and does not depend on the exposure time.

To convert the number of photons into the number of atoms, the photon emission rate of the atom has to be known. Assuming saturated transitions, i.e $I >> I_s$, the maximum photon scattering rate per atom amounts to $\Gamma_{\text{sc}} = \frac{\gamma}{2} 2\pi \approx 18\,\text{MHz}$. Due to the different coupling strengths between the magnetic hyperfine sublevels, the effective saturation intensity can be larger than I_s, thus the scattering rate can be lower by a factor of 2. Apart from errors in the measurement discussed above, the absolute atom number can only be determined within that uncertainty, which is accurate enough to get a coarse estimation for the lower limit of the atom number. The fluorescence signal was measured at at maximum scattering rate, i.e $\delta_0 \approx 0$. For $t_{\text{exposure}} = 250\,\mu$s, this

leads to a conversion factor for the number of atoms per count

$$\eta_{\text{atoms}} = \frac{1}{\Gamma_{\text{sc}} t_{\text{exposure}}} \eta_{\text{photons}} \approx 100 \, \frac{\text{atoms}}{\text{count}}.$$

In contrast to η_{photons}, η_{atoms} depends on the particular exposure time. The uncertainty in the solid angle of the light collection elements leads to an relative uncertainty in the atom number of 20% which is represented by the errorbars in the plots. To be able to measure larger atom numbers, the camera must not be saturated by the signal. For that reason, further measurements of the atom number were performed at a detuning $\delta = -20\,\text{MHz}$, where the fluorescence signal is smaller for the same atom number. The conversion factor for $t_{\text{exposure}} = 250\,\mu\text{s}$ has a value of

$$\eta_{\text{atoms},\delta} = 310 \, \frac{\text{atoms}}{\text{count}}.$$

Most of the measurements were performed at $t_{\text{exposure}} = 750\,\mu\text{s}$ with the corresponding conversion factor

$$\eta_{\text{atoms},\delta} = 103 \, \frac{\text{atoms}}{\text{count}}.$$

Measurements

Two types of measurements are performed: To count the ***total atom number***, the sum over all pixels is calculated after each shot. The pixelsum is proportional to the atom number provided that two assumptions are made:

1. The CCD chip's response is linear with photon number.

2. The fluorescence signal is proportional to the atom number, i.e the atomic cloud is transparent for the emitted photons even at higher atom numbers.

To find a set of parameters where the atom number is largest, one has to be careful: It is not sufficient to optimise the MOT with respect to the highest fluorescence signal of the atoms since their scattering rate and thus their brightness changes with experimental parameters, making statements about the atom number impossible. To compare the atom number after each optimisation step, the experimental parameters are switched to a set of default values, e.g the detuning is ramped to

$$\delta_{\text{MOT}} = -20\,\text{MHz}$$

within 3 ms. Then, a variation within the signal at a fixed scattering rate allows the comparison of absolute atom numbers.

To determine the ***temperature*** of the MOT, a series of time of flight images is taken after the ballistic expansion of the cloud. The hotter the atoms are, the larger is the distance they fly before the image is taken. To resolve the dynamics of the expansion, the atoms have to be illuminated for a period which is small compared to their time of flight and to the relaxation time in the MOT. This can be realized by setting a time window with a camera exposure time of

$$t_{camera} = 500\,\mu\text{s}$$

and turning on the MOT beams via the AOMs for

$$t_{exposure} \approx 10\,\mu\text{s}$$

within that time window. To make sure that the AOMs can be swiched fast enough, we measured the illumination period with a photodiode: $t_{exposure} \approx 10\,\mu$s is realistic number for our AOMs.

4.1. Loading rate and total atom number

As described in chapter 2.2.3, the MOT's loading rate and the maximum total atom number are equivalent properties since the total number of atoms is determined by the equilibrium of atoms loaded into the trap and atom losses. In the following, the measured loading rate as well as its dependence on two experimental parameters is discussed:

1. Parameters of the cooling laser beams: detuning of the MOT lasers δ_{MOT} and Zeeman slower δ_{Slower} and intensity of the Zeeman slower beam.

2. Oven temperature.

Loading curves

The total atom number versus the loading time is shown in figure 4.1 for $T = 300\,^{\circ}\text{C}$ and in figure 4.1 for $T = 400\,^{\circ}\text{C}$.

One can see, that the loading rate of the MOT reaches values of

$$L \approx 10^7\,\frac{\text{atoms}}{\text{s}}$$

for an oven temperature of $T = 300\,^{\circ}\text{C}$ and

$$L \approx 10^9\,\frac{\text{atoms}}{\text{s}}$$

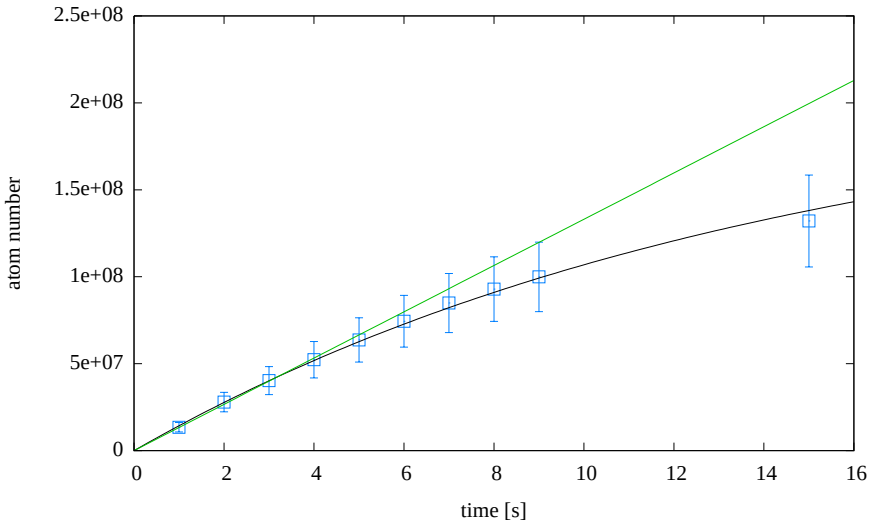

Figure 4.1.: *Loading curve of the MOT at $T = 300\,℃$. The saturation of the atom number is not reached within $t > 15\,s$ loading time. The black fit assumes the rate equation 2.48 for the atom number in the MOT taking losses due to background collisions into account. Two-body losses are neglected. The green line is a linear fit to determine the loading rate to $L \approx 1.5 \cdot 10^7\,atoms/s$. Without two-body losses, the maximum atom number in the MOT is expected to reach $N_{\max} \approx 2 \cdot 10^8\,atoms$. The data points for longer loading rates already indicate, that the atom number saturates earlier. This shows that the maximum atom number is limited by two-body losses (see also figure 4.2).*

for a temperature of $T = 400\,℃$. Compared to an expected flux of

$$L \approx 5 \cdot 10^{11}\,\frac{\text{atoms}}{\text{s}}$$

of trappable atoms for $T = 400\,℃$, the value of the measured flux is one order of magnitude smaller. This can be attributed to the fact that only about half of the atoms entering the Zeeman slower are in the trappable $m_J = +1/2$ ground state while the others are in the $m_J = -1/2$ state (see figure 2.5). Another loss factor of atoms is the effect of transversal heating in the Zeeman slower: During deceleration of the atoms, they gain velocity in the transversal direction. This leads to an additional spread of the atomic beam. As a consequence, a larger number of atoms cannot be trapped by the MOT anymore.

The atomic flux is still large enough to realize an experimental cycle of a few seconds. The loading curves plotted in figure 4.1 and 4.2 show typical signs

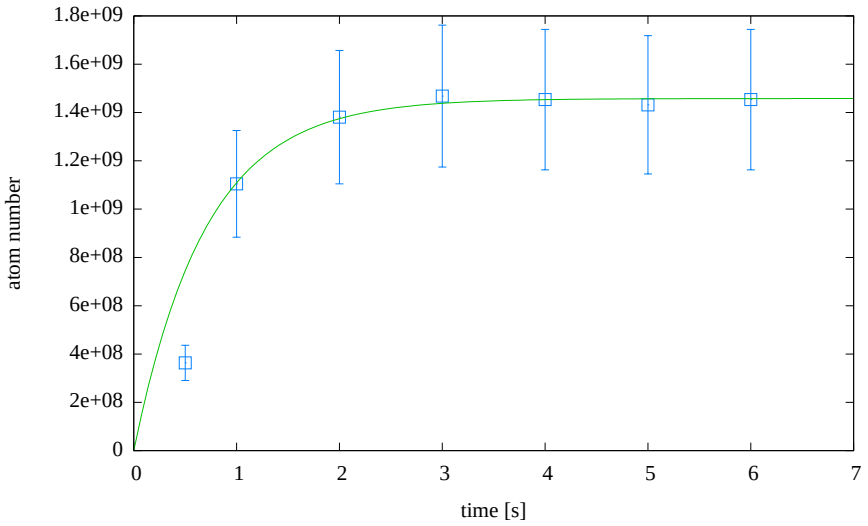

Figure 4.2.: *Loading curve of the MOT at $T = 400$ ℃. The atom number saturates already after $t > 2\,s$ at a maximum value $N_{\max} = 10^9$ atoms. When the one body loss rate R is assumed to be similar to the one body loss rate $R \approx 10^{-3}$ 1/s in the case when the atomic beam is blocked (see figure 4.6), the maximum atom number in the MOT considering only one-body losses would yield $N_{\max} = L/R \approx 10^{12}$ atoms. The saturation already at $N = 10^9$ atoms shows the strong domination of two-body losses over trap losses due to background gas atoms.*

of dominant loss factors in the MOT: Both at $T = 300\,℃$ and $T = 400\,℃$the maximum atom number saturates at values much lower than predicted by the one-body model, where the maximum atom number is given by $N = L/R$ with one-body lossrate R.

Laser detunings and beam intensities

The detuning of the Zeeman slower with respect to the detuning of the MOT beams depends on the frequency of the sound wave propagating in the Zeeman slower AOM. In our experiment, it has a fixed value of

$$\delta_{\text{Slower}} = \delta_{\text{MOT}} - 70\,\text{MHz},$$

because the angle of the beam leaving the AOM in the first refraction order depends on the frequency of the sound wave: After changing its frequency, the Zeeman slower beam has to be coupled into the fibre again. Before the MOT

was loaded, it was completely cleared by closing the Zeeman slower beam and the cooler beam for a short time. Then, the MOT was loadet for 0.5 s at an oven temperature of $T = 300\,℃$ and a detuning δ_{MOT}. To compare the absolute atom numbers for the different detunings, the MOT detuning is ramped to a default value of

$$\delta_{image} = -20\,\mathrm{MHz}$$

where the pictures are taken. Figure 4.3 shows the dependence of the atom number on the detuning. The increase in atom number for larger detunings

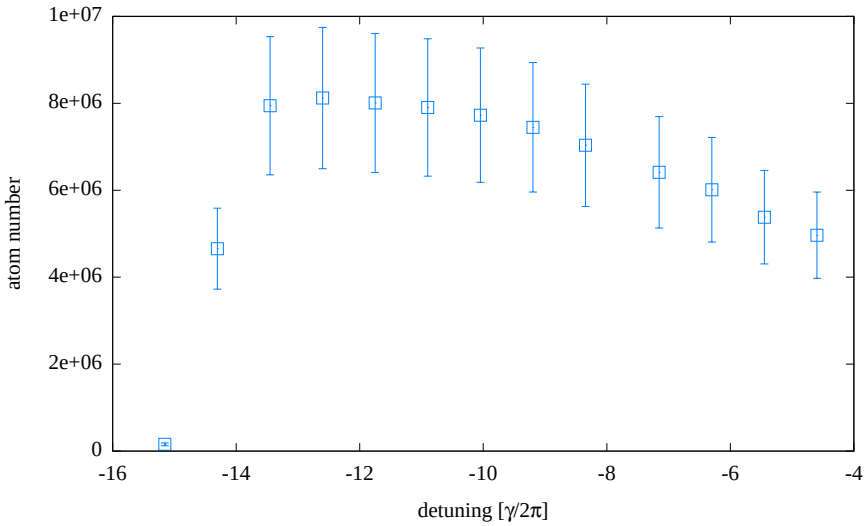

Figure 4.3.: *Dependence of the atom number in the MOT on the detuning of the MOT beams at $T = 300\,℃$ and $t_{load} = 0.5\,s$. The loading rate increases with larger detunings since the detuning of the Zeeman slower beam is shifted by the same amount. By that means higher capture velocities of the Zeeman slower can be reached providing an increase in the atomic flux. The optimum value for the detuning is found to be $-11\gamma < \delta < -13\gamma$. When the detuning gets too large, the atom number drops abruptly. This indicates a too large effective detuning of the Zeeman slower at some point. As a consequence, the atoms escape the deceleration process at too high velocities and are not capturable by the MOT anymore.*

can be explained according to the remarks in section 2.2.3:

1. Larger detunings of the Zeeman slower allow an increase in capture velocities and increase in atomic flux since the slower's capture velocity is

given by:

$$v_c^{\text{Slower}} \propto -\delta_{\text{Slower}} + const \cdot B.$$

2. As explained in section 2.2.3, larger detunings allow a higher capture velocities of the MOT. By that means the time of flight between the Zeeman slower and the centre of the MOT decreases. Thus the spread of the atomic beam after the Zeeman slower is decreased. This leads to a higher number of trappable atoms.

When the detuning is increased over a certain value, the atom number drops abruptly. This can be explained by the following effect: When the detuning of the Zeeman slower deviates too much from the design value, the scattering rate at critical positions within the slower is likelely to be too low for further deceleration of the atoms. When this happens at too high velocities, the atoms cannot be trapped by the MOT anymore.

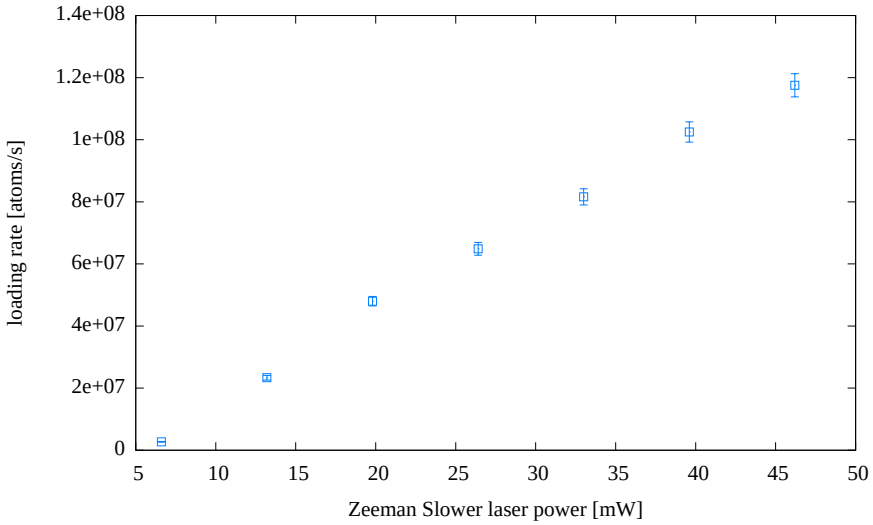

Figure 4.4.: *Dependence of the MOT loading rate on the power in the Zeeman slower beam at* $T_{\text{oven}} = 300\,℃$. *An increase in intensity of the Zeeman slower laser beam would lead to a higher loading-rate.*

The dependence of the loading rate on the power in the Zeeman slower laser beam is plotted in figure 4.4. The linear dependence suggests, that not enough photons are available to slow all the atoms. To check this for $T_{\text{oven}} = 400\,℃$, the photonic flux can be estimated. To decelerate one atom from

$$v_{initial} = 1000\,\frac{\text{m}}{\text{s}}$$

to

$$v_{end} = 10\,\frac{\mathrm{m}}{\mathrm{s}}$$

at half of the maximum scattering rate

$$a = a_{max}/2 \approx 100000\,\mathrm{m/s^2}$$

can be estimated in the following way: The time to decelerate one atom is calculated to

$$t = \frac{v_{initial} - v_{end}}{a} \approx 10^{-3}\,\mathrm{s}.$$

With a conservative estimation for the scattering rate

$$\gamma_{eff} = 1/2\gamma_p = 1/4\gamma = 1/4 \cdot 2\pi \cdot 5.87 \cdot 10^6\,1/\mathrm{s} \approx 9 \cdot 10^6\,1/\mathrm{s},$$

it takes approximately $N = 9 \cdot 10^3$ photons to stop one atom. With available laser power $P = 45\mathrm{mW}$, a photonic flux of

$$f_{\mathrm{photons}} = \frac{\hbar\omega}{P} \approx 1.5 \cdot 10^{17}\mathrm{photons/s}$$

can be reached. With that value of the photonic flux, an atomic flux of

$$f_{atoms} = \frac{f_{\mathrm{photons}}}{9 \cdot 10^3} \approx 10^{16}\,\mathrm{atoms/s}$$

should be trappable. Hence, the linearity in the loading rate with laser power in the Zeeman slower beam has to be attributed to another effect. The real reason is unknown at the moment.

Oven temperature

The temperature of the effusive lithium oven is the parameter which influences the loading rate strongest: The dependence of the atom number on the oven temperature is plotted in figure 4.5 for a loading time $t_{\mathrm{load}} = 0.5\,\mathrm{s}$. The exponential increase in the partial pressure in the oven leads to an exponential increase in number densities providing a higher atomic flux. For our setup, this behaviour can not be extrapolated to higher temperatures due to the following reasons:

1. Higher densities in the MOT lead to an increase in two-body losses. So the maximum atom number saturates earlier for higher temperatures.

2. As described in chapter 2.2.2, higher oven temperatures lead to higher transversal velocities of the atoms. So a smaller amount of atoms leaving the oven is trappable by the MOT.

For 450 °C, a saturation effect is already visible at a rather short loading time $t_{load} = 0.5\,\mathrm{s}$ of the MOT.

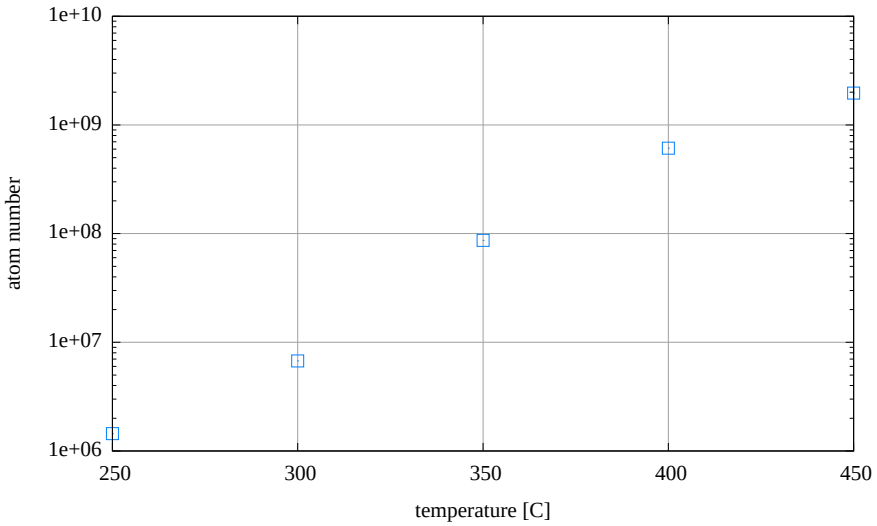

Figure 4.5.: *Dependence of the atom number on the oven temperature at a loading time $t_{load} = 0.5\,s$. Due to the exponential increase of the number density of atoms in the oven with increasing temperature, the loading rate also increases exponentially up to a temperature of 400 ℃. At higher temperatures $T \approx 450$ ℃, higher densities are reached and loss channels like two-body collisions dominate.*

It can be clearly seen in figure 4.6, that the maximum atom number in the MOT is limited by two-body losses. After loading the MOT, the Zeeman slower laser beam is blocked and the atomic beam shutter is closed. The remaining atoms are imaged after several storage times reaching up to 700 s. Two regimes can be distinguished: During shorter storage times $t < 150\,\mathrm{s}$, a strong non-exponential behaviour is visible. Within that time, the sample decays more than exponentially ("super-exponential"). This indicates the presence of two-body losses which scale according to equation 2.46 with n^2. This model is confirmed by the the fit to the super-exponential decay 2.50

$$N(t) = N_0 \frac{Re^{-Rt}}{R + N_0\beta'(1 - e^{-Rt})}$$

which agrees well with the measured data. The fit parameters are listed in table 4.1.

Initial atom number	N_0	$(3 \pm 0.3) \cdot 10^8$atoms
Two-body loss coefficient	β'	$(5 \pm 0.5) \cdot 10^{-10} \frac{1}{\mathrm{s\,atom}}$
Decay rate super exponential decay	R	$(1.1 \pm 0.3) \cdot 10^{-3} \frac{1}{\mathrm{s}} \mathrel{\widehat{=}} (900 \pm 250)\,\mathrm{s}$
Decay rate exponential decay	R	$(2.6 \pm 0.5) \cdot 10^{-3} \frac{1}{\mathrm{s}} \mathrel{\widehat{=}} (500 \pm 100)\,\mathrm{s}$

Table 4.2.: *Fit parameter of figure 4.6. A lower limit for the lifetime of the sample is given by the fit parameter for the exponential decay. A more realistic value can be determined by the fit parameter of the super-exponential decay (equation 2.50):* $\tau \approx 15$ *minutes.*

The lifetime of the sample is limited by high densities during the time of measurement. In the regime $t > 300$s, the decay behaviour is still not exponential, but the influence of background collisions becomes visible. The fit parameter for the exponential decay neglecting two-body losses

$$N(t) = N_0\, e^{-R \cdot t}$$

gives a lower limit for the lifetime $\tau = 1/R$, whereas the fit parameter for the decay 2.50, which is stronger than exponential, is expected to be closer to the real lifetime of the sample with

$$\tau \approx (900 \pm 250)\,\mathrm{s}.$$

4.2. Temperature

After having optimised the parameters such that a high atom number is obtained, the next optimisation goal is a low temperature to trap as many atoms as possible in the optical dipole trap. The two main parameters to control the temperature of the atomic sample are the following:

1. Detuning: Recalling equation 2.22, in an optical molasses the temperature scales linearly for large detunings :

$$k_B T = \frac{\hbar\gamma}{4} \frac{1 + (2\delta/\gamma)^2}{(|\delta|/\gamma)}$$

and has a minimum for $\delta = \gamma/2$. To take this effect into account, the detuning is ramped from large values to $\delta = \gamma/2$.

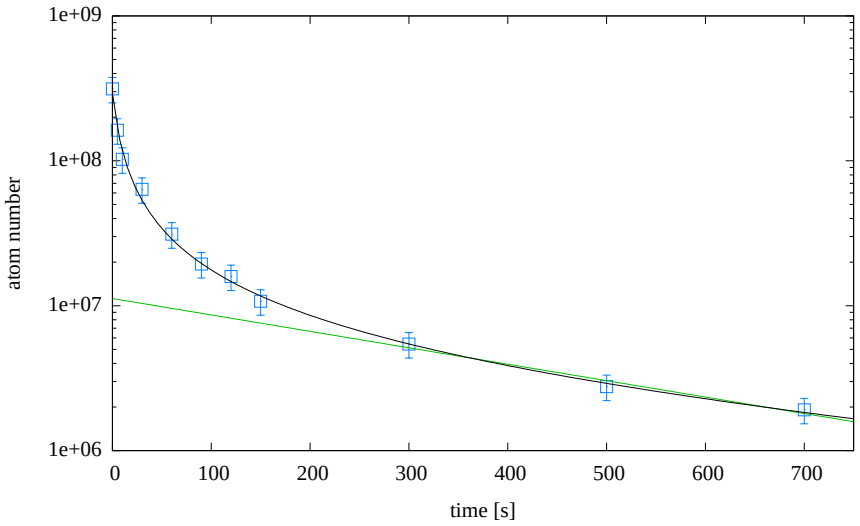

Figure 4.6.: *Atom number in the MOT after closing the atomic beam shutter at* $T_{\text{oven}} = 400\,℃$. *The lifetime of the atomic sample at high densities is limited by two-body losses indicated by the strongly non exponential behaviour for short times. For longer storage times, the lifetime is limited by collisions with the background gas resulting in an exponential decay. This regime is not yet reached. The black curve is a fit to the decay which is stronger than exponential 2.50. An estimation for the lifetime can be given from the decay rate of the exponential fit curve* $\tau > (500 \pm 100)\,s$, *but it is expected to be as long as the time constant of the super exponential decay* $\tau \approx (900 \pm 250)\,s$. *This shows an extremely good background pressure of the setup.*

2. Laser intensities: As discussed in section 2.1.3, the minimum temperature T_D can only be reached when the heating rate is equal to the cooling rate. This is only given when $\delta = \gamma/2$, but the heating rate can be reduced by decreasing the laser intensities. While ramping the detuning closer to resonance, the laser intensities of cooler and repumper are ramped down simultaneously. To prevent cooler atoms from taking part in the cooling cycle again, they are transferred into the $\left|^2S_{\frac{1}{2}}, F = 1/2\right\rangle$ dark state by ramping down the repumper faster than the cooler leading to a decrease in heating rate.

The atom number is very sensitive to the ramping speeds of detuning and laser intensities. In particular, too high end values of cooler and repumper intensities at small detunings force the atoms to escape the trap in an uncon-

trolled manner and too early. Nevertheless, parameters for low temperatures and good signal to noise ratios have been found: The MOT loads at an oven temperature of $T = 350\,℃$ for $t = 3\,\mathrm{s}$ to collect enough signal for a good signal-to-noise ratio. The cloud is released from the trap by ramping down the MOT laser beams within 2.7 ms and decreasing the detuning at the same time. After a time of flight ranging from $20\,\mu s \leq t_{tof} \leq 2000\,\mu\mathrm{s}$, the camera exposures for $500\,\mu\mathrm{s}$. Within that time window, the atomic cloud is illuminated for $10\,\mu\mathrm{s}$ by switching the MOT laser beams with the aoms. The time of illumination has to be as short compared to the time of flight of the atoms, because otherwise the light would alter the spatial distribution of the atoms. To check where this effect plays a role, the time of illumination could be increased up to $100\,\mu s$ before seeing the influence of the light.

The size of the atomic cloud at that point in time is determined by a gaussian fit to its density distribution. As seen in section 2.2.3, the trapping potential in a MOT is harmonic. The energies of the thermal cloud in the trap obey Boltzmann statistics so the density distribution forms a gaussian:

$$n(\mathbf{r}) = n_0 e^{-\frac{U(\mathbf{r})}{k_B T}} = n_0 \exp - \sum_{i=1}^{3} x_i^2/(2\sigma_i) \tag{4.1}$$

with $1/\sqrt{e}$ width $\sigma_i = 1\sqrt{k_B T/\kappa_i}$. When the trap is switched off, the atoms begin to expand ballistically.

The energies of the atoms in the expanding cloud also obey Boltzmann statistics:

$$P(\mathbf{p})d\mathbf{p} \propto e^{-\frac{\frac{\mathbf{p}^2}{2m}}{k_B T}} d\mathbf{p} \tag{4.2}$$

An atom starting from position $\mathbf{r}_0$ and arriving at position $\mathbf{r}$ after a time of flight t has a momentum

$$\mathbf{p} = m(\mathbf{r} - \mathbf{r}_0)/t.$$

So equation 4.2 can be rewritten as the probability for the atom to arrive at fixed position $\mathbf{r}$ when it started at position $\mathbf{r}_0$

$$P(\mathbf{r}_0)d\mathbf{r}_0 \propto e^{-\frac{\frac{m^2(\mathbf{r}-\mathbf{r}_0)^2}{2mt^2}}{k_B T}} d\mathbf{r}_0. \tag{4.3}$$

To obtain an expression for the density distribution after a time of flight t, one has to weight the initial spatial distribution of the atoms $n(\mathbf{r}_0)$ with the probability for the atom to arrive at position $\mathbf{r}$

$$P(\mathbf{r}_0)d\mathbf{r}_0$$

and integrate over all possible initial positions $\mathbf{r}_0$

$$n(\mathbf{r},t) = \int P(\mathbf{r}_0,t)n(\mathbf{r}_0)d^3\mathbf{r}_0 = \int e^{-\frac{m^2(\mathbf{r}-\mathbf{r}_0)^2}{2mt^2k_BT}} e^{-\frac{\mathbf{r}_0^2}{2\sigma_0^2}} d^3\mathbf{r}_0. \tag{4.4}$$

The convolution of the two Gaussians forms a gaussian and its $1/\sqrt{e}$ width is just the inverse sum of the convoluted Gaussians:

$$\sigma_i = \sqrt{\sigma_i(t=0) + \frac{k_BT}{m}t^2} \tag{4.5}$$

To get a better signal to noise ratio, the sum over all single columns of the time of flight pictures has been taken. A gaussian is fitted to the density distribution of each image. The fit is performed in realtime within the LABVIEW user interface of the computer control. This has the advantage that optimisations of the parameters with respect to temperature can directly be controlled. The expansion of the atomic cloud versus its time of flight is plotted in figure 4.7.

To determine the temperature of the atoms, equation 4.5 is fitted to the data points in figure 4.7 over the whole time of flight (green line). The temperature has been determined from the fit parameter to

$$T \approx 470\,\mu K.$$

For an estimation of the error, following effect has to be taken into account: The magnetic fields of the MOT cannot be switched off on a timescale which is short compared to the time of flight of the atoms. The influence of the magnetic potential on the expansion of the cloud can be estimated as follows: The acceleration due to the magnetic potential in the axis with strong field gradient is given by

$$a = \frac{F}{m} = \frac{m_F g_F \mu_B \frac{\partial B}{\partial z}}{m}. \tag{4.6}$$

For the $F = 3/2, m_F = 3/2$ state, the acceleration in the strong axis of the magnetic field gradient is largest:

$$a \approx +\frac{3}{2}\cdot\left(-\frac{1}{3}\right) g_J\mu_B\frac{\partial B}{\partial z}m \approx -\frac{9.3^{-28}\mathrm{J/Gauss}\cdot 40\,\mathrm{Gauss/cm}}{10^{-26}\mathrm{kg}} \approx -370\,\mathrm{m/s^2}$$

The influence of the acceleration on the flight distance of the atoms is given by kinematics:

$$x(t) = v_0t + 1/2\,a\cdot t^2 \tag{4.7}$$

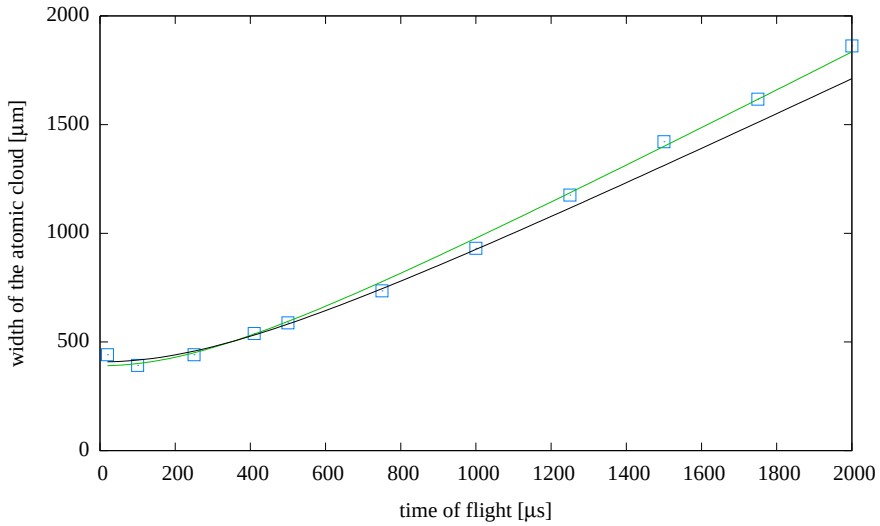

Figure 4.7.: *Temperature measurement of atoms in the MOT. The width of the atomic cloud is plotted versus its time of flight: After their release from the trap, the atomic cloud expands according to its initial velocity which is a measure for the temperature of the atoms. To record their expansion, the atomic cloud is illuminated for* $10\,\mu s$ *by the MOT laser beams for several time of flights. Each data point represents the width of a gaussian fit to the density distribution of the cloud. The green line is a fit to equation 4.5. over the whole x-axis. To reduce the systematic error in the measurement (see text), the black curve takes only values for short time of flights* $0 < t < 1$ *ms into account. A lower limit for the temperature is determined within a factor of three (conservative estimation, see text) by the fit parameter to* $T = 410\,\mu K$*.*

Inserting the values of our measurement $v_0 = 0.7\text{m/s}$ at $T = 470\,\mu K$ and $t = 2\,\text{ms}$, one gets for the flight distance

$$x = 1.4\,\text{mm} - 0.8\,\text{mm}.$$

Hence, the magnetic field introduces an error of 130% for the velocity if just one data point at $t = 2\,\text{ms}$ was taken. In this case, only an upper limit for the temperature of the sample can be estimated within a factor of 4.

One expects, that the measured value is more precise than the error suggests, since the deceleration for the other hyperfine states $F = 3/2 m_F = +1/2$ and $F = 1/2 m_F = -1/2$ is a factor of two smaller.

In addition, the error becomes smaller for shorter time of flights. At $t = 1\text{ms}$

$$x = 0.80\,\text{mm} - 0.40\,\text{mm},$$

reducing the error to 200% for one single data point. To get an estimation for the temperature as precisely as possible, the best strategy is to take as many data points as possible for shorter time of flights $t < 1\,\mathrm{ms}$. For those reasons, a second fit (black line) in figure 4.7 accounts only for values $0 < t < 1\,\mathrm{ms}$. According to the discussion for the error above, the temperature could determined within a factor of three to

$$T = 410\,\mu K.$$

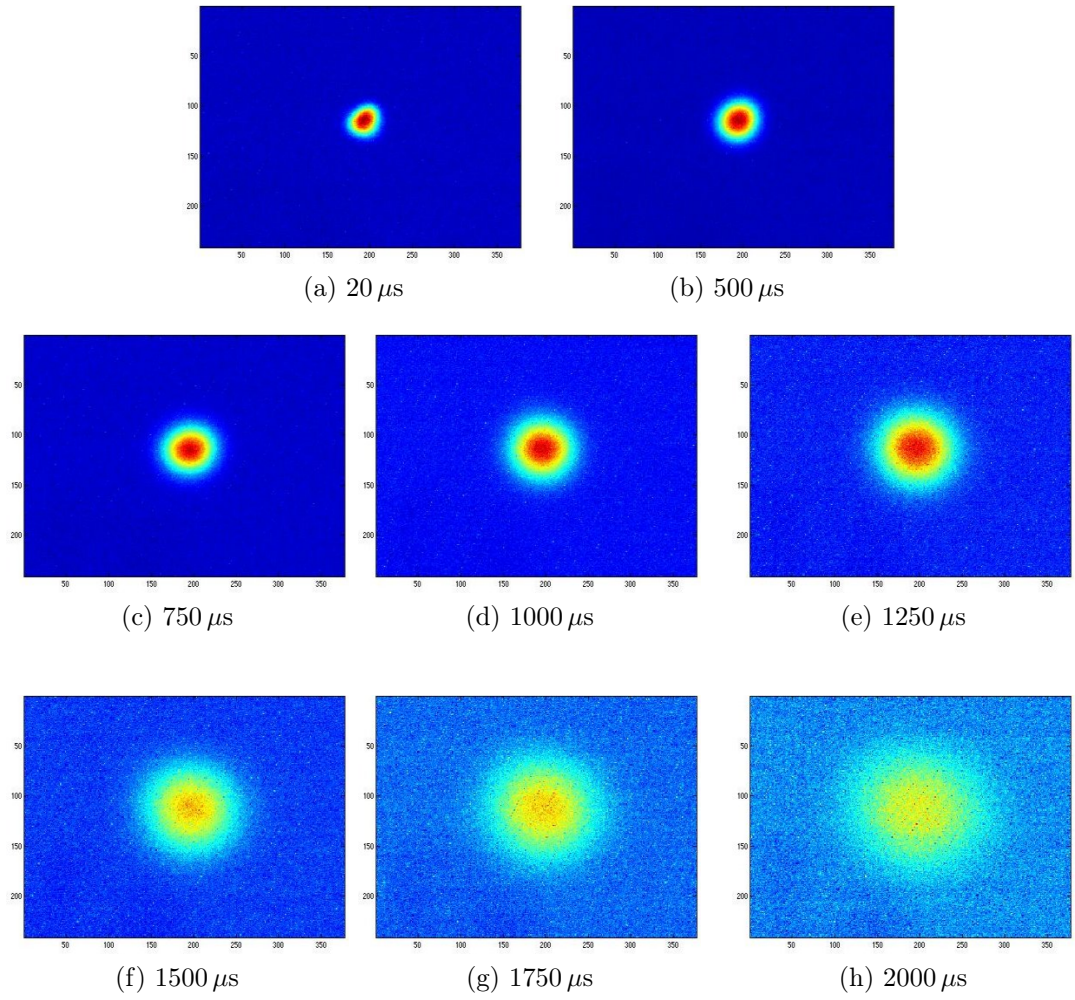

(a) 20 μs (b) 500 μs

(c) 750 μs (d) 1000 μs (e) 1250 μs

(f) 1500 μs (g) 1750 μs (h) 2000 μs

Figure 4.8.: *Expansion of the atomic cloud for several times of flight. The scale of the axes is adjusted to map the aspect ratio of the cloud 1:1. The total width of an image measures 2.5 mm.*

5. Conclusion and outlook

The aim of this thesis was the setup of a Magneto-Optical-Trap as a step towards the preparation of a degenerate Fermi gas. The work focusses on two main subjects: the design and implementation of a Zeeman slower providing a source of slow atoms for the MOT and the setup up of a vacuum chamber according to the specific prerequisites for experiments dealing with a small number of ultracold fermions. The following experimental goals for the apparatus could be reached:

1. The constructed Zeeman Slower provides the capacity to load $\approx 10^9$ atoms into the MOT within 1 second at an oven temperature of 400°C. Since the MOT loading rate is a bottleneck for the whole experimental cycle, a total duration of a few seconds finally seems to be reachable.

2. The vacuum in the experimental chamber meets the demands in so far, that losses of the ultracold atomic sample due to background collisions limit the lifetime to ≈ 15 minutes. This is much longer than the planned duty cycle of the experiment promising a long living mesoscopic fermionic system.

After optimisation, the temperature of the atoms in the MOT was measured to $T \approx 410\mu$K. This value is low enough to reach high transfer efficiencies for the atoms from the MOT into the optical dipole trap. Following steps towards the preparation of a degenerate mesoscopic Fermi gas have to be taken: To reach degeneracy in a Fermi gas, i.e every state is occupied by one identical fermion, the phase space density defined as

$$n\lambda^3_{\text{De Broglie}}$$

with De Broglie-wavelength $\lambda_{\text{De Broglie}} = \sqrt{\frac{2\pi\hbar}{mk_BT}}$ has to become on the order of 1.

With lowest temperatures and highest densities in the MOT reachable, only phase space densities on the order of $n\lambda^3_{\text{De Broglie}} \approx 10^{-4}$ can be obtained. Thus

another cooling method has to be applied: the atoms are cooled evaporatively by lowering the trap depth of the optical dipole trap. Evaporative cooling of fermions and the preparation of molecular Bose-Einstein condensates are established techniques today to reach highly degenerate macroscopic Fermi gases [4][5][6]. The challenge in the preparation of a few atom gas is posed by the control on the atom number. Once a large degenerate Fermi gas is prepared, unwanted atoms can be poured out of the trap by means of a magnetic field gradient. The more the energy levels are separated in the trap, the better is the control on the number of remaining atoms. Large dipole traps make the pouring process difficult: The shape of a typical dipole trap becomes very shallow after the evaporation process, similar to a plate. Thus the atom number in the trap becomes too sensitive to applied magnetic field gradients. In contrast, the potential formed by a tightly focused optical dipole trap (waist $w \approx 1\,\mu m$) has well separated energy levels. Here, the energy level spacing is on the order of the Fermi energy. Spilling of the trap leads to a well defined number of remaining atoms. For those reasons, an optical microtrap is the appropriate tool to prepare a mesoscopic system. In first experiments one would test, how precisely the atom number can be defined by the spilling method. Furthermore the minimum number of atoms in the sample has to be determined.

5.1. Towards a model system

As adumbrated in the introduction, an idea for first experiments towards a model for few fermion systems will be discussed shortly in the following. A degenerate Fermi gas consisting of only few atoms is expected to show typical properties: In analogy to the electrons of an atom, the trapped fermions in the gas occupy single-particle states. Due to the fermionic nature of the particles, energy shells develop. When the number of particles in the system is just large enough to fill a shell, a "magic number" is reached: Then the binding energy per particle is expected to become maximal. The formation of energy shells can be observable, when a sample with a small, well defined atom number can be prepared: The energy of the sample can be determined similar to the time-of-flight measurements for the temperature in the MOT. The energy of the sample depending on the atom number should unveil the shell structure: Adding atoms to the sample where all shells are closed could lead in a measureable increase in energy of the sample. A theoretical approach demonstrated by the group of Chris Greene[25] suggests this: According to their calculations, the motion of the gas can be described via a single coordinate R, i.e the extension rms

radius of the sample. The problem can be reduced to a 1-D linear Schrödinger equation with an effective potential

$$V_{\text{eff}}(R) = \frac{(3N-1)(3N-3)}{8MR^2} + \frac{\lambda(\lambda+3N-2)}{2MR^2} + \frac{1}{2}\omega^2 R^2 + V_{\text{int}} \tag{5.1}$$

with the appropriate hyperangular momentum quantum number λ and trap frequency ω. The energy term V_{int} accounts for two-body s-wave interactions. The radius of the sample can be determined from the minimum of the effective potential 5.1. In the non-interacting case, one obtains for the rms radius

$$\left\langle R^2 \right\rangle = \left(\frac{\lambda}{N} + \frac{3N}{2}\right) l_0^2 \tag{5.2}$$

with oscillator length $l_0 = \sqrt{\hbar/m\omega}$ and for the energy

$$E_{\text{NI}} = (\lambda + \frac{3N}{2})\hbar\omega. \tag{5.3}$$

The magic numbers for the first 5 shells are listed in table 5.1.

filled shells	atom number	λ
1	2	0
2	8	3
3	20	60
4	40	90
5	70	210

Table 5.1.: *Magic numbers for the first 5 energy shells. The appropriate quantum number is the hyperangular momentum λ. Taken from [25].*

Including interactions, the behaviour of the system becomes even more interesting: Then the interaction term in the effective potential 5.1 has to be taken into account. After the renormalization of the two-body s-wave interaction [9], the effective potential has the shape plotted in figure 5.1 (dashed curves). As expected, the radius of the atomic cloud shrinks with increasing attraction. The system is predicted to be stable even in the limit of maximum attraction (s-wave scattering length a$\rightarrow -\infty$).

In contrast, a Fermi gas consisting of 3 or more components is expected to behave completely different: The effective potential for a 3 component Fermi gas has a weak hyperradial barrier, similar to the dotted curve in figure 5.1. Such a gas is predicted to collapse in the limit of strong attractive interactions, which has to be proved experimentally.

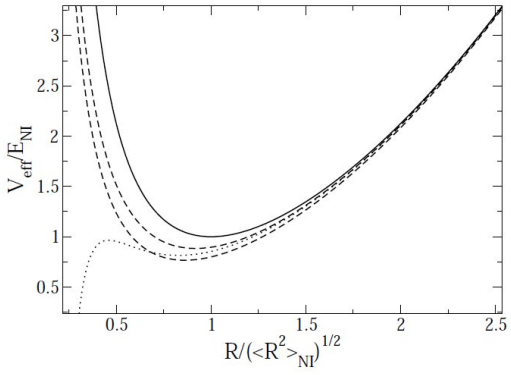

Figure 5.1.: *The dimensionless ratio of the effective potential to the non interacting energy is plotted as function of the rescaled rms radius. The solid curve shows the noninteracting case whereas the dashed curves include attractive interactions. Calculations were performed for a degenerate Fermi gas consisting of two species (hyperfine states). Top to bottom increasing attraction. Taken from [9].*

A. Technical drawings

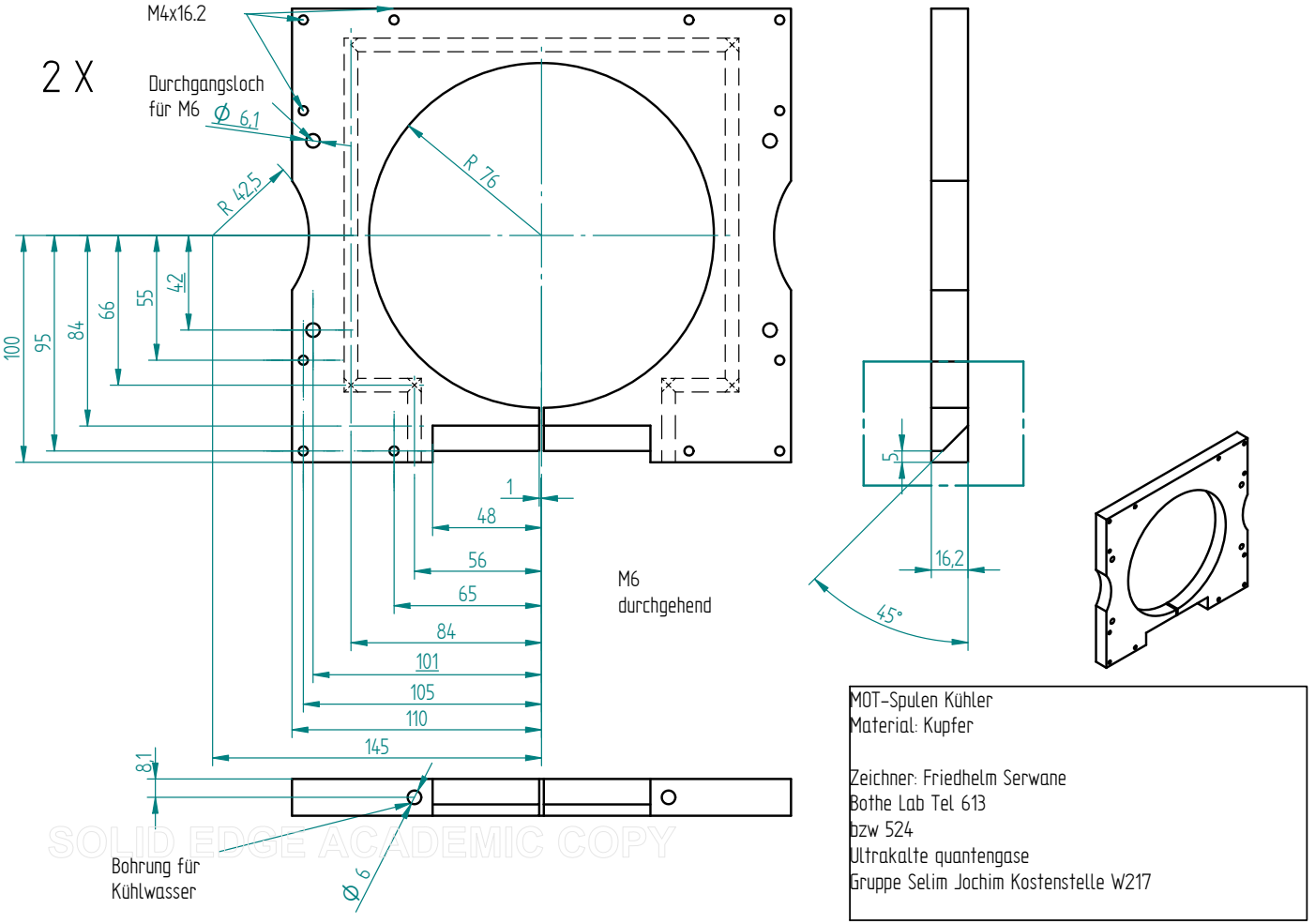

Figure A.1.: *Water cooling system for the MOT coils.*

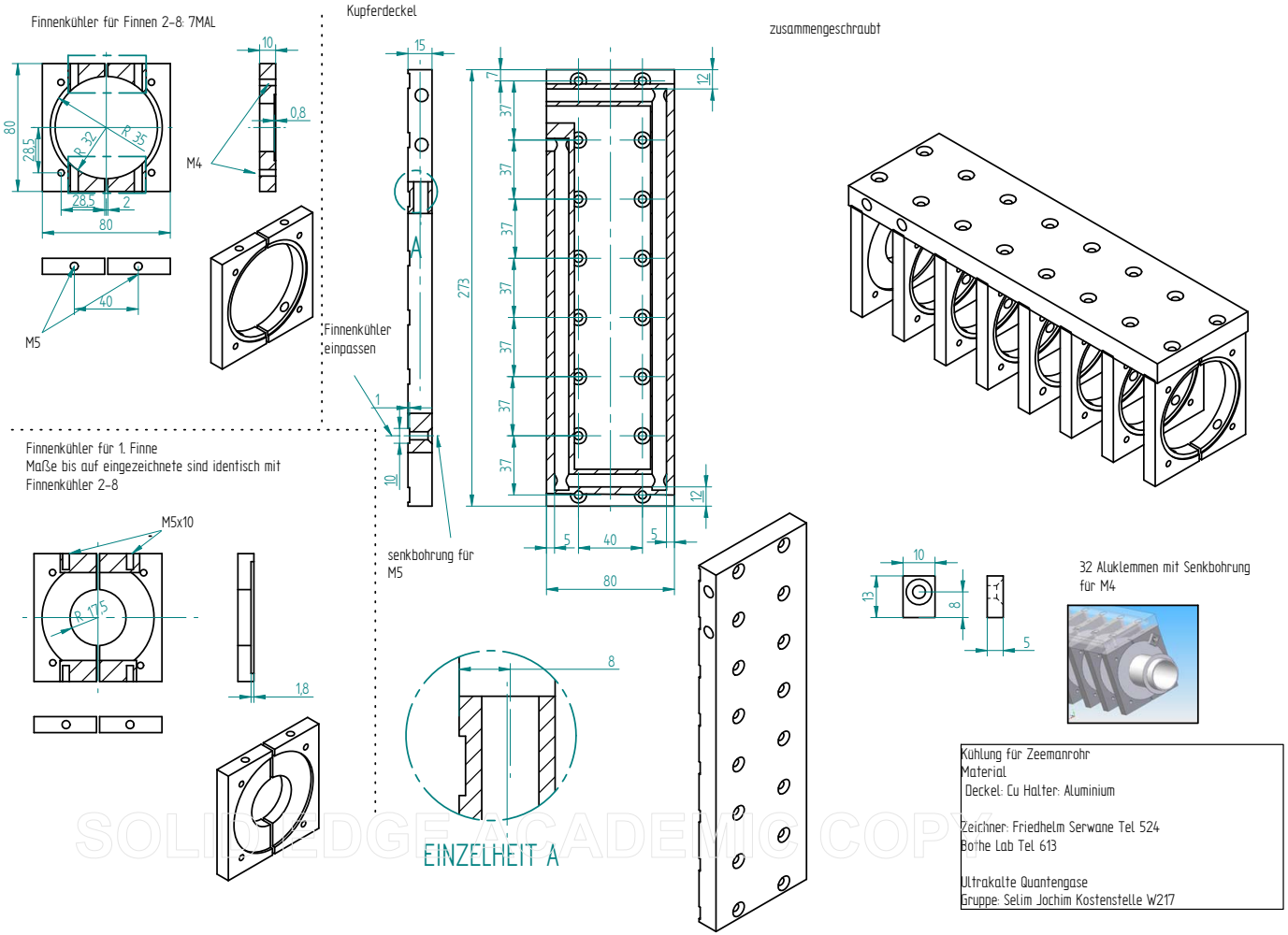

Figure A.2.: *Water cooling system for the Zeeamn slower.*

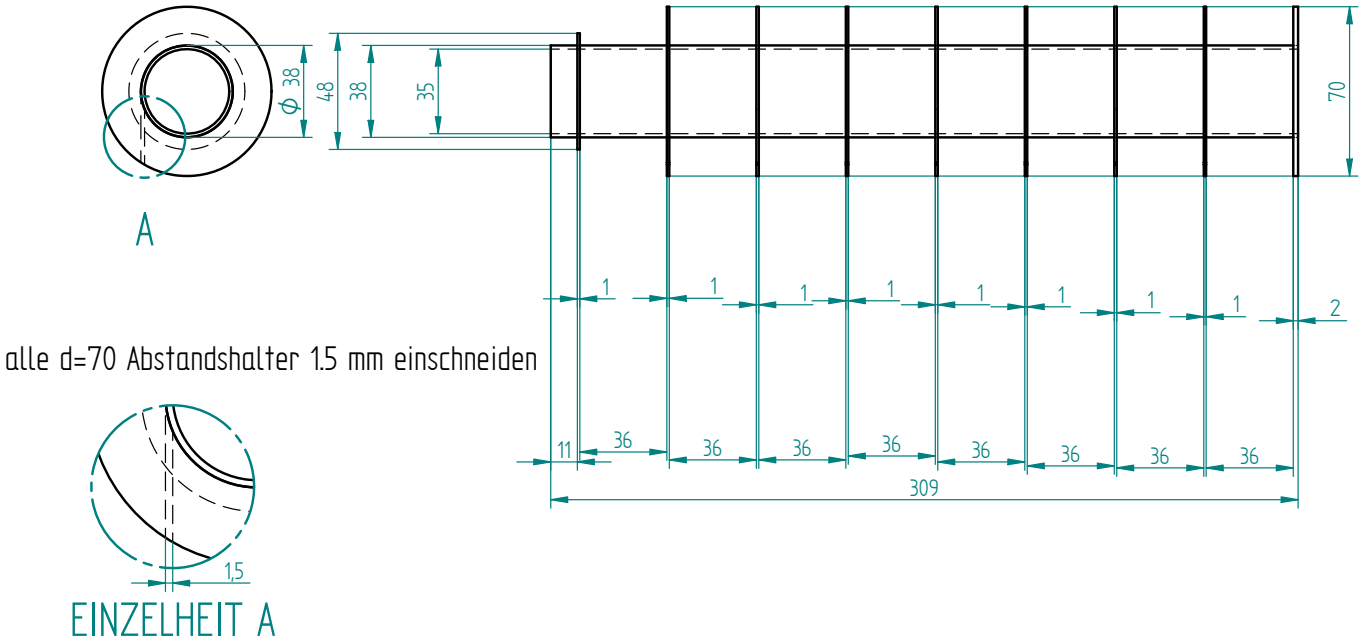

Figure A.3.: *Mount for the Zeeman Slower Coils.*

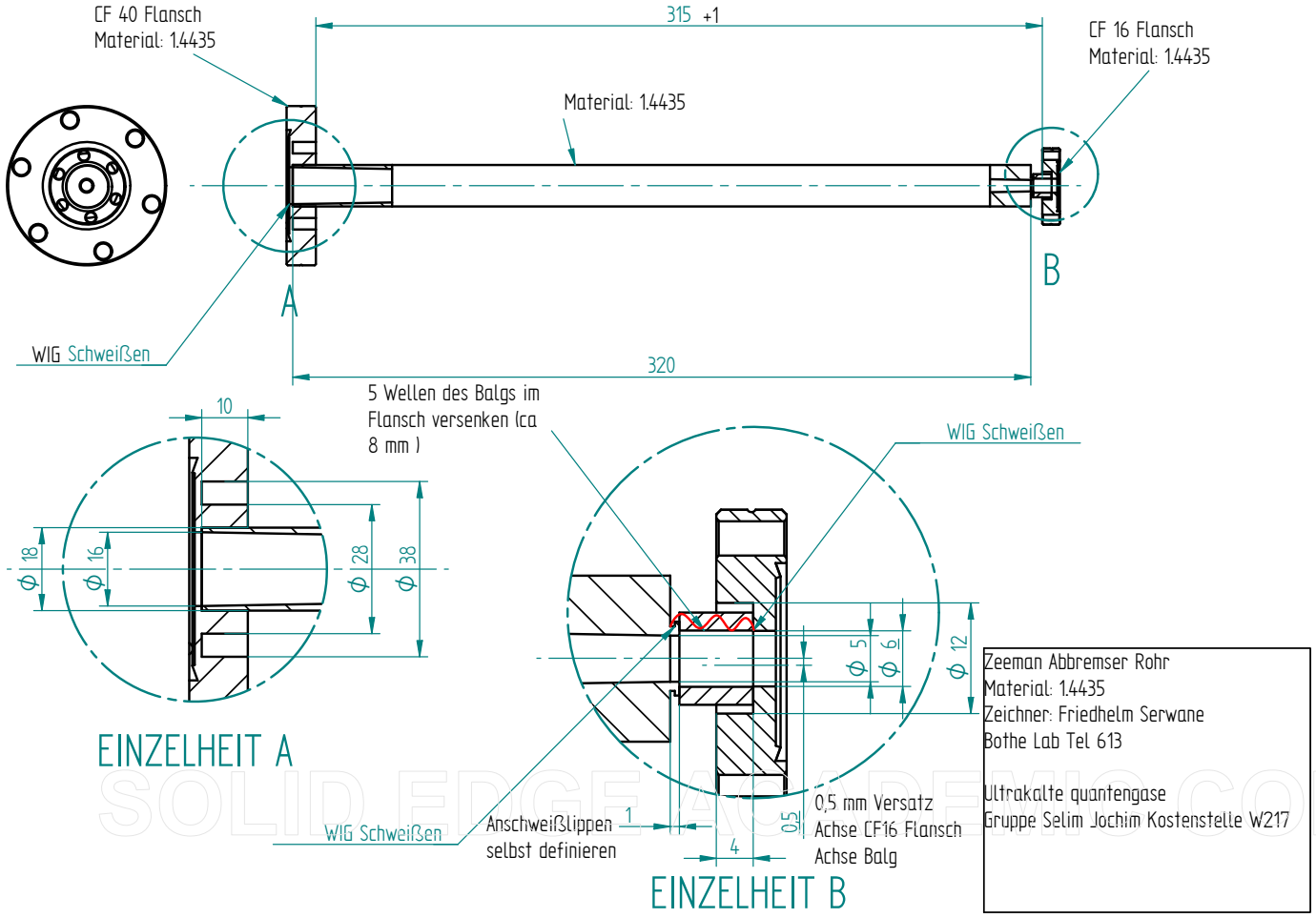

Figure A.4.: *Conical Zeeman slower tube.*

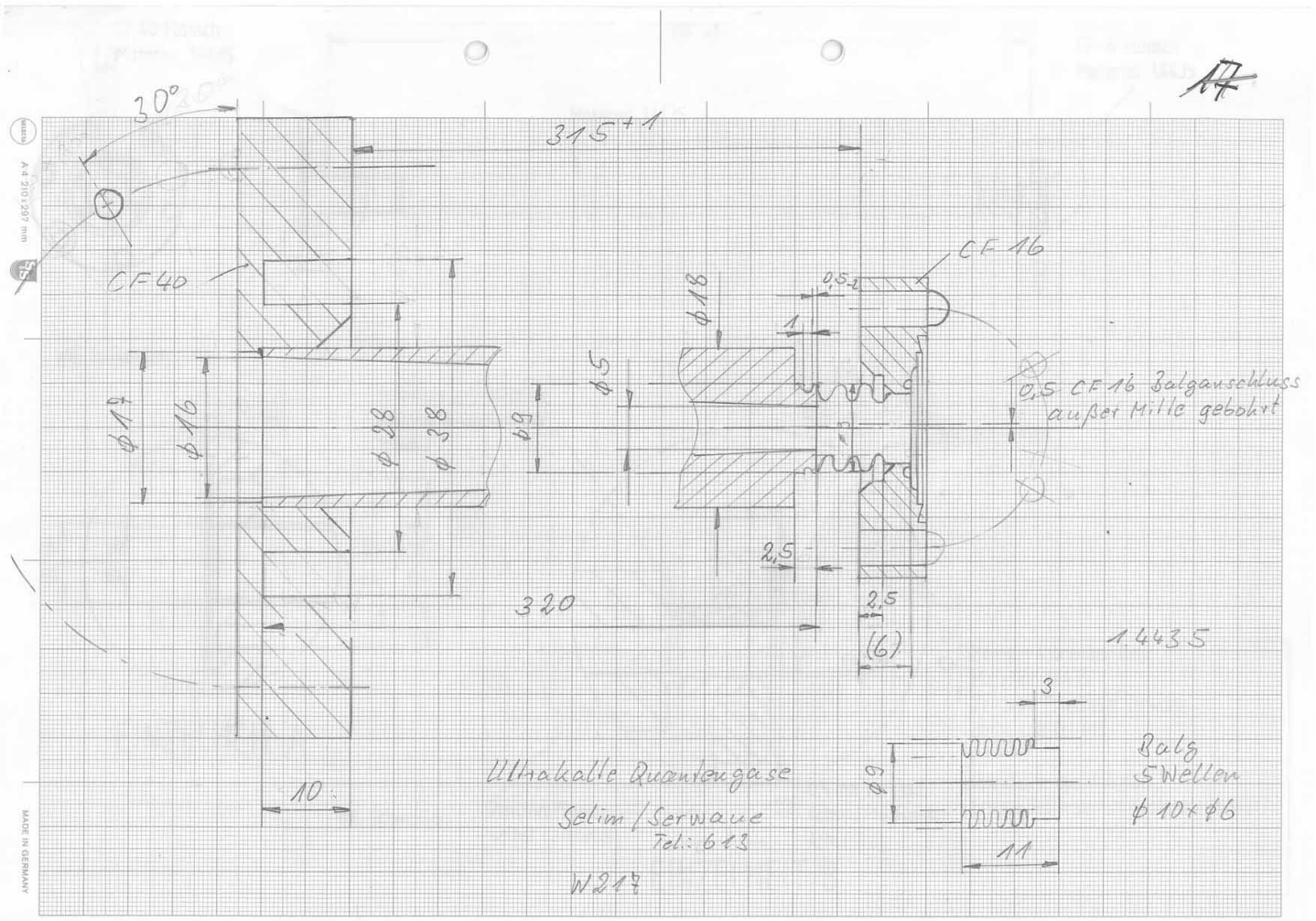

Figure A.5.: *Details on the bellow of the conical Zeeman Slower tube. Drawing: Mallinger.*

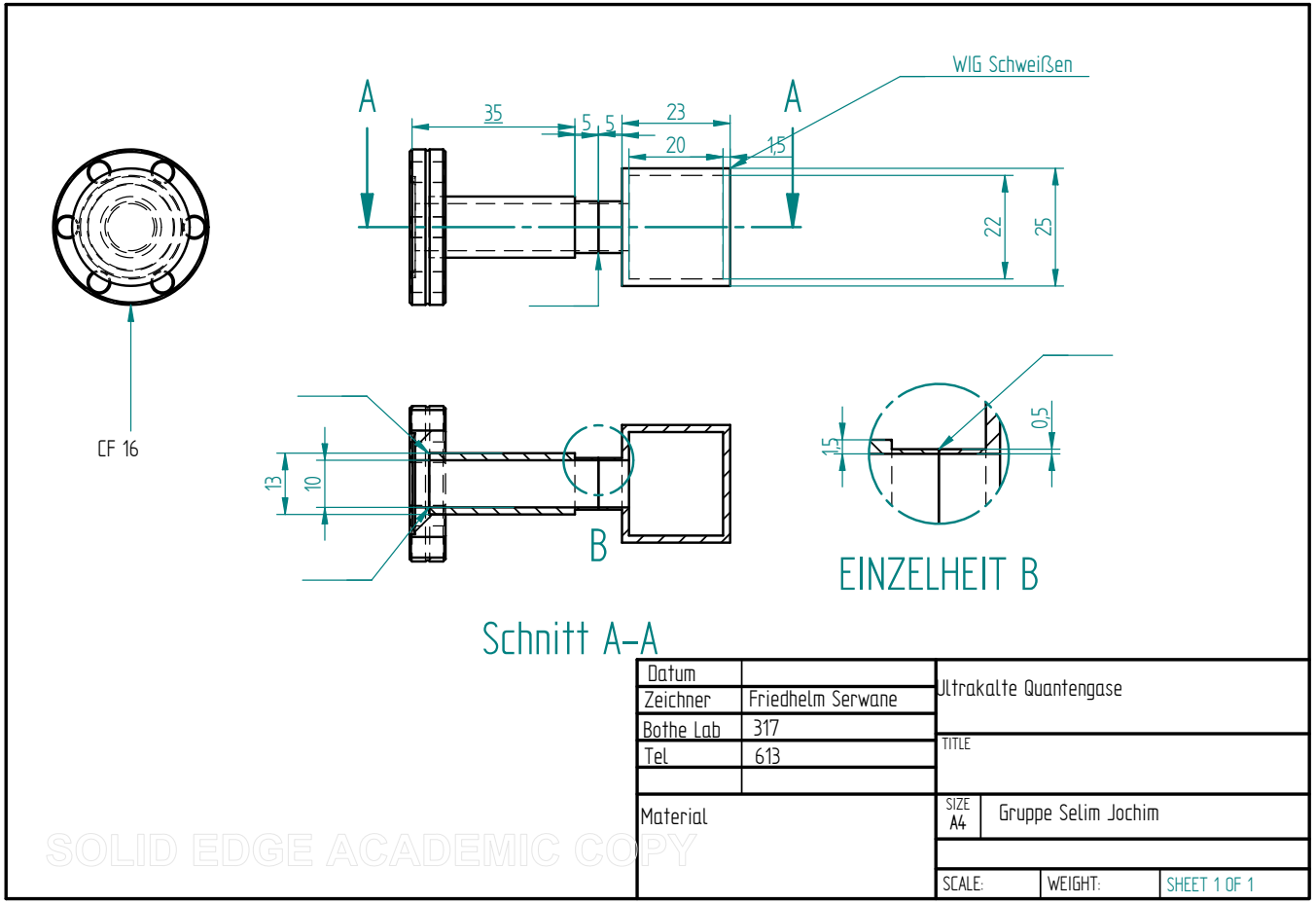

Figure A.6.: *Effusive lithium oven.*

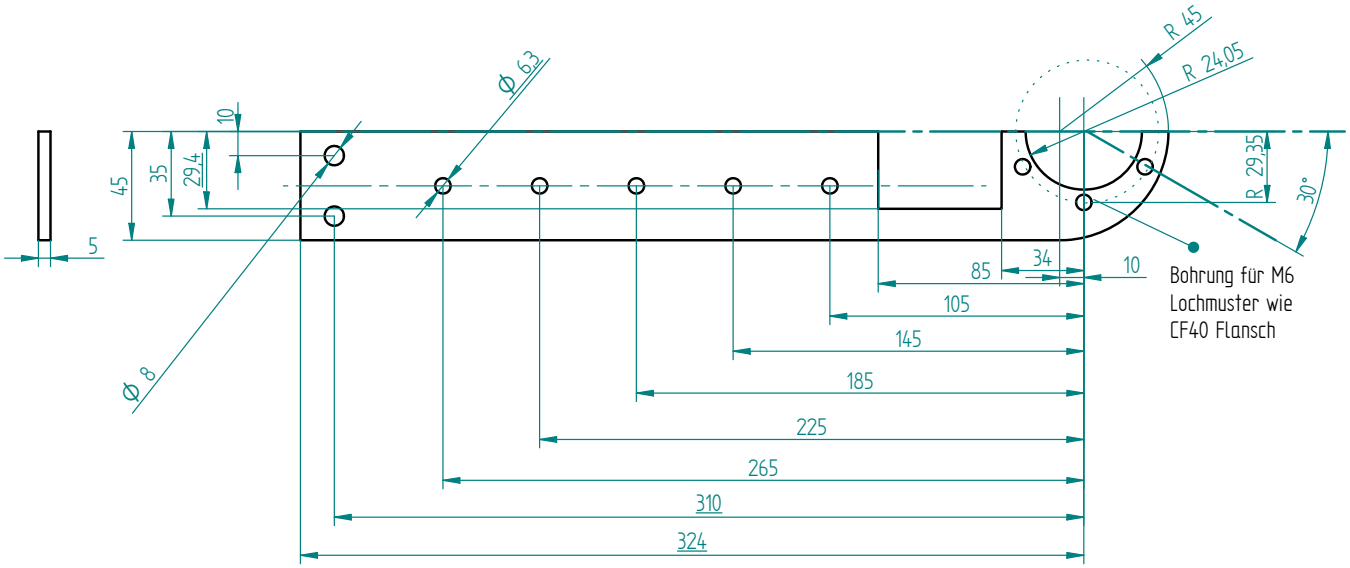

4 X

Halterung Octagon Material: Edelstahl
Zeichner: Friedhelm Serwane
Bothe Lab Tel 613
, bzw 524
Ultrakalte quantengase
Gruppe Selim Jochim Kostenstelle W217

Figure A.7.: *Mounting clamps for the octagon.*

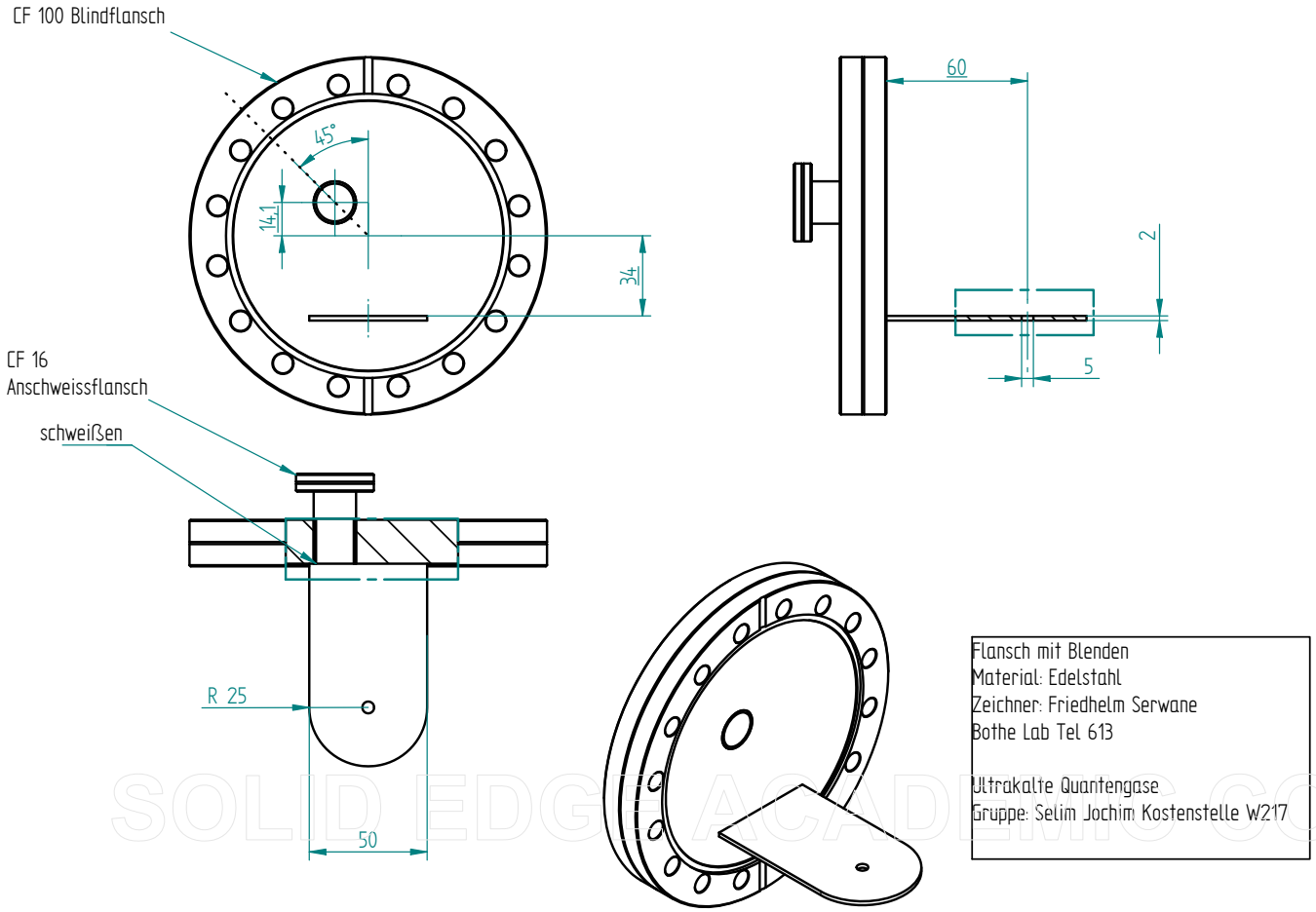

Figure A.8.: *Vacuum feedthrough.*

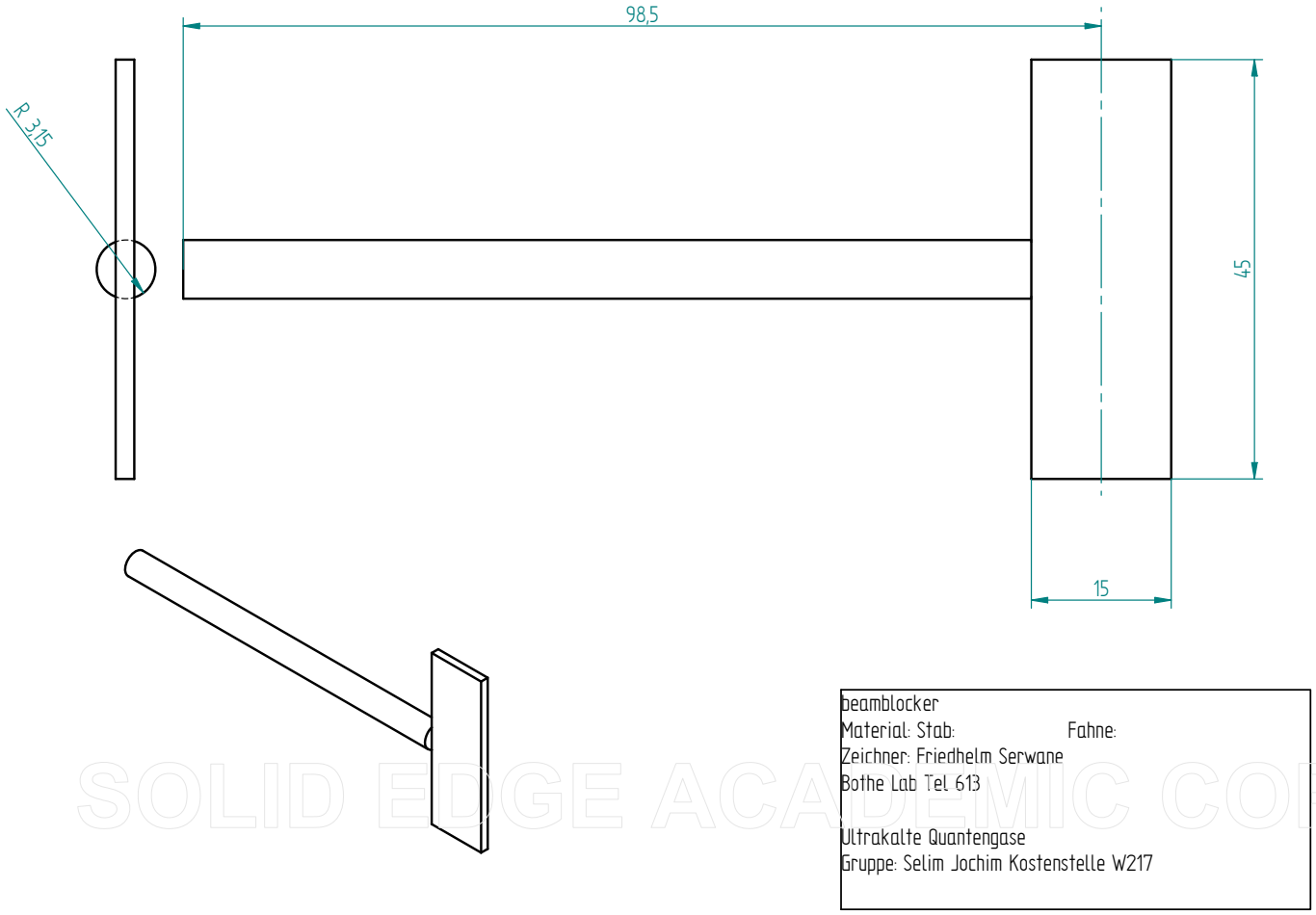

Figure A.9.: *Atomic beam shutter.*

Bibliography

[1] M. H. Anderson, J. R. Ensher, M. R. Matthews, C. E. Wieman, and E. A. Cornell. Observation of bose-einstein condensation in a dilute atomic vapor. *Science*, 269:198, 1995.

[2] M. R. Andrews, C. G. Townsend, H.-J. Miesner, D. S. Durfee, D. M. Kurn, and W. Ketterle. Observation of interference between two bose-einstein condensates. *Science*, 275:637, 1997.

[3] B. DeMarco and D. S. Jin. Onset of Fermi Degeneracy in a Trapped Atomic Gas. *Science*, 285(5434):1703–1706, 1999.

[4] S. Jochim, M. Bartenstein, A. Altmeyer, G. Hendl, S. Riedl, C. Chin, J. Hecker Denschlag, and R. Grimm. Bose-einstein condensation of molecules. *Science*, 302:2101, 2003.

[5] Markus Greiner, Cindy A. Regal, and Deborah S. Jin. Emergence of a molecular bose-einstein condensate from a fermi gas. *Nature*, Nov 2003.

[6] M. Wand Zwierlein, C. A. Stan, Schunck. C. H., S. M. F. Raupach, S. Gupta, Z. Hadzibabic, and W. Ketterle. Observation of bose-einstein condensation of molecules. *Phys. Rev. Lett.*, 91(25):250401, Dec 2003.

[7] M. Zwierlein, J. R. Abo-Shaeer, A. Schirotzek, C. H. Schunck, and W. Ketterle. Vortices and superfluidity in a strongly interacting fermi gas. *Nature*, 435:1047, Jul 2005.

[8] S. Chu, J. E. Bjorkholm, A. Ashkin, and A. Cable. Experimental observation of optically trapped atoms. *Phys. Rev. Lett.*, 57:314, 1986.

[9] Seth T. Rittenhouse and Chris H. Greene. The degenerate fermi gas with renormalized density-dependent interactions in the k harmonic approximation, 2007.

[10] Rudolf Grimm, Matthias Weidemuller, and Yurii B. Ovchinnikov. Optical dipole traps for neutral atoms. *MOLECULAR AND OPTICAL PHYSICS*, 42:95, 2000.

[11] J. Dalibard and C. Cohen-Tannoudji. Dressed-atom approach to atomic motion in laser light: the dipole force revisited. *J. Opt. Soc. Am. B*, 2(11):1707, 1985.

[12] Harold J. Metcalf and Peter van der Straten. *Laser Cooling and Trapping*. Springer-Verlag, New York, 1999.

[13] Schunemann, Engler, Zielonkowski, Weidemuller, and Grimm. Magneto-optic trapping of lithium using semiconductor lasers. *Optics Communications*, 158(11):263, 1998.

[14] M. E. Gehm. *Preparation of an Optically-Trapped Degenerate Fermi Gas of ^{6}Li: Finding the Route to Degeneracy*. PhD thesis, Duke University, 2003.

[15] J. Steinmann. *Multiphoton Ionization of Laser Cooled Lithium*. PhD thesis, Heidelberg University, 2007.

[16] M. E. Gehm. Properties of ^{6}Lithium, 2003: *http://www.phy.duke.edu/research/photon/qoptics/techdocs/pdf/PropertiesOfLi.pdf*.

[17] Thomas Alan Savard. *Raman Induced Resonance Imaging of Trapped Atoms*. PhD thesis, Duke University, 1998.

[18] G. Scoles. *Atomic and molecular beam methods*, volume 1. Oxford University Press, 1988.

[19] Wutz-Adam-Walcher. *Theorie und Praxis der Vakuumtechnik*, volume 1. Vieweg, 1988.

[20] W. Demtröder. *Laserspektroskopie*. Springer Verlag, Berlin, Heidelberg, New York, 1993.

[21] P. S. Julienne and Jacques Vigué. Cold collisions of ground- and excited-state alkali-metal atoms. *Phys. Rev. A*, 44(7):4464–4485, Oct 1991.

[22] K. M. O'Hara, S. R. Granade, M. E. Gehm, T. A. Savard, S. Bali, C. Freed, and J. E. Thomas. Ultrastable co_2 laser trapping of lithium fermions. *Phys. Rev. Lett.*, 82(21):4204–4207, May 1999.

[23] Neg: Non evaporable getter coating: *http://est-div-sm.web.cern.ch/est-div-sm/Project-Getter-home.htm*.

[24] Mathematica notebook to calculate magnetic fields: *http://www.phy.duke.edu/research/photon/qoptics/techdocs/tools/Coils.nb*.

[25] Seth T. Rittenhouse, M. J. Cavagnero, Javier von Stecher, and Chris H. Greene. Hyperspherical description of the degenerate fermi gas: s-wave interactions. *Physical Review A (Atomic, Molecular, and Optical Physics)*, 74(5):053624, 2006.

Acknowledgements

I would like to thank everybody who supported me during this year. Especially following persons:

Juniorprofessor Selim Jochim
for all the excellent supervision I had this year. I could learn a lot of things from him, not only in physics.

Timo Ottenstein, *Thomas Lompe*, *André Wenz*, and *Jochen Steinmann*
for the proofreading and the support of my thesis.

My colleagues
for the answers to so many questions.

Prof. Ullrich and his group
for the pleasant and inspiring atmosphere at the MPI.

Prof. Wolf
as the second reviser of this thesis.

The MPI Tischfußball-team
for the numerious battles.

Furthermore I wish to thank

Gerda Serwane
for her courage during the last 25 years.

Karl Serwane
for his crazy ideas.

Felix Serwane
for cleaning our kitchen.

Mechtild Hartmann and *Karl Schnekenburger*
not only for the good dinners I had with them.

Julia Hartmann
for everything.

Erklärung:

Ich versichere, dass ich diese Arbeit selbstständig verfasst und keine anderen als die angegebenen Quellen und Hilfsmittel benutzt habe.

Heidelberg, den _____ _____

Unterschrift